energies

MDPI

Article

Discrete vs. Discretized Control in Voltage Source Inverters for UPS Systems

Zbigniew Rymarski *, Wojciech Oliwa and Grzegorz Wieczorek

Department of Electronics, Electrical Engineering and Microelectronics, Faculty of Automatic Control, Electronics and Computer Science, Silesian University of Technology, 44-100 Gliwice, Poland; woliwa@polsl.pl (W.O.); gwieczorek@polsl.pl (G.W.)

* Correspondence: zrymarski@polsl.pl

Abstract

Digital control in UPS systems is currently the only reasonable way of controlling a voltage source inverter (VSI). The control frequency range is restricted to up to about 1 kHz owing to the output low-pass LC filter, which should also maintain the output voltage during one switching period for the step unload. The measurement channels in the low-pass frequency range can be modeled as delays equal to some switching periods. A reasonably high (about 50 kHz) switching frequency minimizes the delays of the measurement channels. Two control systems will be compared—the pure discrete control, in this case a one-sample-ahead preview deadbeat control (OSAP), and a discretized passivity-based control (PBC). The OSAP control is easy to realize, is very fast, and enables one to obtain a steady state in a restricted number of steps after disturbance. However, the single-input single-output deadbeat control version is useless because it depends very strongly on the parameters of the inverter. The multi-input single-output OSAP (MISO-OSAP) control is directly based on discrete state equations (we treat the output voltage, output current, and inductor current as the measured state variables) and works perfectly for the nonlinear rectifier RC load (PF = 0.7) in a system without delay. The version of this with a linear prediction of state variables by means of a full-order state Luenberger observer (MISO-OSAP-LO) will be used in systems with different delays and compared with the discretized MISO passivity-based control without prediction for relatively high switching frequency (about 50 kHz). The aim and the novelty of the paper are in enabling a choice between one of these control systems for high switching frequency VSI with delays in the measurement channels.

Keywords: voltage source inverter; deadbeat control; one-sample-ahead preview control; passivity-based control; multi-input single-output control; Luenberger observer

check for updates

Academic Editor: Tek Tjing Lie

Received: 30 April 2025
Revised: 8 June 2025
Accepted: 19 June 2025
Published: 25 June 2025

Citation: Rymarski, Z.; Oliwa, W.; Wieczorek, G. Discrete vs. Discretized Control in Voltage Source Inverters for UPS Systems. *Energies* **2025**, *18*, 3336. https://doi.org/10.3390/en18133336

Copyright: © 2025 by the authors. Licensee MDPI, Basel, Switzerland. This article is an open access article distributed under the terms and conditions of the Creative Commons Attribution (CC BY) license (https://creativecommons.org/licenses/by/4.0/).

1. Introduction

The basic problem for traditional control design is in creating the object model and describing it with state equations. In the case of a voltage source inverter, it can be simply presented as an RLC circuit—the output LC filter model—because of the relatively low bandpass and much higher switching frequency f_s. The digital PWM modulator always introduces one switching period delay, and the measurement channels are forms of low-pass filters (with a bandpass below the Nyquist frequency) that can be treated as a delay in the low bandpass of the output LC filter. A comparison between a very fast, purely discrete (a continuous version does not exist) multi-input single-output one-sample-ahead preview (MISO-OSAP) controller (deadbeat type) [1–3], with or without the full-order

state Luenberger observer [4,5] (MISO-OSAP-LO) for state variables prediction, and a discretized MISO passivity-based controller (MISO-PBC) that is designed to be used for systems requiring supervision of their internal energy (previous research has proved the controller's significant utility for inverters [6]), will be shown. The discrete model of an inverter, based on the solution of continuous equations that describe the inverter for switched-on and switched-off bridge transistors over one switching period, accurately describes said inverter by taking into account the type of the PWM modulator (e.g., the additional delay in the double-edge modulation caused by the influence of the previous pulse width on the current switch-off time). This model is directly used in MISO-OSAP control. The MISO-PBC control calculates the internal energy of the inverter and could, theoretically, be slower. The idea of the paper is to proceed with the comparison of these two controls. The novelty of this paper is in its proposal of a better choice for UPS systems with relatively high switching frequencies, one based on the requirements of IEC 62040-3:2021 [7]. Meanwhile, previous work has proved that state variable prediction is not necessary for MISO-PBC at this switching frequency (about 50 kHz) [8]. The rectifier RC load [7] (with power factor (PF) = 0.7, calculated according to C.I. Budeanu's theory) was used for testing, as it is the most universal test of a control system. The pure dynamic test results (20–100–20% of the nominal resistive load) depend more on the inverter output capacitor than on the control system (Section 2).

In Section 2, experimental inverter models are described, including the inverter bridge parameters and simplified Bode plots of the measurement channels. In Section 3, a discrete model of the inverter with a three-level double-edge PWM is presented. In Section 4, a simulation of a VSI with a discrete one-sample-ahead preview controller—MISO deadbeat—with or without a prediction unit is performed. In Section 5, a VSI with a discretized version of the improved MISO passivity-based control is simulated. Section 6 presents the discussion of the simulation results. In Section 7, experimental models with OSAP and PBC controls are tested and compared. In Section 8, there is a discussion of the experimental verification results, and Section 9 contains conclusions.

2. The Tested Inverter

First, the output LC filter parameters should be calculated. We can assume that the highest amplitude of harmonics in the output PWM voltage should be below the assigned level, i.e., below 3%, with a THD below 5% [9], or below 8% according to the requirements of the IEC 62040-3:2021 standard [7] concerning UPS systems. The highest harmonic frequency is equal to or close to the switching frequency [10]. The idea of the minimization of the sum of the absolute values of the reactive powers in the filter inductor and capacitor (this sum is a kind of "cost function"), together with the restriction of the highest amplitude of harmonics, is presented in [11]. There are similar approaches for creating the "cost function" from the absolute values of powers, e.g., [12], but with different coefficients for the reactive powers. Here, the absolute value of the reactive power in the filter inductor was typically found to have a coefficient over unity [12]; this is because the authors wanted to increase the capacitor and decrease the inductor, whose value restricts the dynamics of the inverter [12]. The inverter output impedance depends mainly on the filter inductor L_F for the low frequencies. The first condition for filter parameters can be described as (1), where the highest amplitude of the harmonic h_{max} with a frequency equal to the switching frequency f_s or for $f_s \pm f_m$ (f_m is the fundamental 50 Hz frequency) is found to be that for the PWM duty ratio, $\tau = 0.5$.

$$\left(h_{max}|_{\tau=0.5}/h_1\right)_{OUT} < 3\% \tag{1}$$

From (1) for the single-phase 3-level double-edge PWM, we receive the approximated condition (2)

$$L_F C_F = \frac{1}{f_s^2} \tag{2}$$

To calculate the specific values of the filter parameters, the cost function *CostF* (3), after substituting (2) into it, should be used.

$$CostF \approx \omega_m(L_F I_{LFh1rms}^2 + C_F V_{LFh1rms}^2) = \omega_m(L_F I_{LFh1rms}^2 + \frac{1}{L_F f_s^2} V_{OUTh1rms}^2) \tag{3}$$

For $I_{LFh1rms} \approx I_{OUTh1rms}$ and $f_s >> f_m$

$$\frac{\partial CostF}{\partial L_F} \approx \omega_m \left(I_{OUTh1rms}^2 - \frac{1}{L_F^2 f_s^2} V_{OUTh1rms}^2 \right) \tag{4}$$

By looking for the minimum of the cost function $\frac{\partial CostF}{\partial L_F} = 0$ and using Equation (2), we obtain Solutions (5) and (6).

$$L_F = \frac{1}{f_s} \frac{V_{OUTh1rms}}{I_{OUTh1rms}} \tag{5}$$

$$C_F = \frac{1}{f_s} \frac{1}{V_{OUTh1rms}/I_{OUTh1rms}} \tag{6}$$

However, Equations (5) and (6) are calculated for the steady-state operation of the inverter. The EN 62040-3 [7] standard defines the nonlinear rectifier RC load with power factor PF = 0.7 and the dynamic linear load with step-down from 100% to 20% of the nominal load and step-up from 20% to 100% for the UPS systems below 3 kW. Let us assume a 5 A step decrease. The inverter feedback has at least a delay of one switching period of a discrete PWM modulator. The calculated width of the pulse is stored in the registers and is applied in the next period. The double-edge modulation has an additional structural delay because the time difference between the current pulse and the previous one depends on the control in the previous period. For the load current step-down, all the excessive current (assumed to be constant in one switching period) from the filter inductor (treated as the current source) flows to the output capacitor. If we assign the output overvoltage Δv_{OUT} = 5 V, switching frequency f_s = 50 kHz (T_s = 20 µs), the step current decrease Δi_{OUT} = 5 A, $C_F = T_s \Delta i_{OUT}/\Delta v_{OUT}$, C_F = 20 µF. In all the presented simulations and measurements of the experimental models: switching frequency f_s = 51,200 Hz, inductor L_F = 2 mH, the coil core is made of the alloy-powder high-quality material MS-Sendust (Micrometals Anaheim, CA, USA) [13], C_F = 51 µF Metallised Polypropylene capacitor WIMA (WIMA GmbH & Co. KG, Mannheim, Germany) MKP 4 (five parallel capacitors 10 µF and one 1 µF for special tests). The serial equivalent resistance of the inverter R_L (the only noticeable variable parameter [14,15] for the constant switching frequency) depends on the power losses in the coil core, the dynamic and static losses on the switching transistors, and all the other serial resistances of the PCB and connectors. The bridge transistors are MOSFET IRFP360LC (Vishay Siliconix, Vishay Electronic GmbH, Selb, Germany) switches driven by IR2184 (International Rectifier, El Segundo, CA, USA) circuits. The serial drain-source on-state resistance is 200 mΩ. It always conducts two serially connected transistors, so this is 400 mΩ. It was assigned the R_L = 1 Ω for serial equivalent resistance. The serial resistance of the MKP capacitor C_F was neglected. The rectifier RC load is: R_s = 1 Ω,

C = 430 µF, R = 100 Ω, the power factor PF ≈ 0.7 [7]. For the high-quality coil core of choke L_F and MKP type C_F, we can assume that L_F and C_F are approximately constant [15] for the constant f_s = 51,200 Hz switching frequency.

There is one more condition for the maximum value of the filter inductor L_{Fmax}. The value of the filter inductor L_{Fmax} should be small enough so that, for the filter input voltage step $\Delta v_{FIN} = V_{DC}$ (1-Msin ($\omega_m t_{RON}$)) at time t_{RON} at the filter input (when the load rectifier begins conduct), the forced increase in the inductor current (controlled by feedback) enables the inverter output to follow the reference sinusoidal voltage (for the rectifier RC load) after the rectifier diode begins conducting (it was approximated $\omega_m t_{RON} = \pi/4$, M is a modulation index, $M \leq 1$). After analysis, we have the approximated relation (7) [16].

$$L_{Fmax} < \frac{(R_L + R_s)\left(\frac{\sqrt{2}}{M} - 1\right)}{\omega_m} \tag{7}$$

For R_L = 1 Ω, serial rectifier resistance R_s = 1 Ω and M = 0.7, L_{Fmax} = 6.4 mH. The calculated maximum value is higher than used in the inverter model (L_F = 2 mH). There are a lot of other approaches to appointing the output filter parameters. In [17], the authors, for a selected cutoff frequency of an output LC filter, analyze L-to-C combinations for different loads and propose a design criterion for the L-to-C filter combination. However, the final result of the required L_F/C_F is similar to the ratio of (5) to (6). The paper [18], 14 years later, is almost the same as [17] and presents the same results. In [19], the authors analyze the inverter output LC filter, calculating the total harmonic distortion (THD) of the output voltage. The final calculations of the filter parameters in [19] depend on the filter quality factor but give similar values of L_F and C_F as in this paper. The authors of [20] propose the analytical calculation of the required inductance of an LC filter in a single-phase full-bridge inverter controlled with a unipolar switching pattern based on filter inductor ripple current estimation. This is a similar approach to [10,11]. In [21] authors minimize the filter reactive power at the maximum load. In all the papers, the results of the output filter parameters calculations are more or less similar to the ones presented in this paper.

Figure 1 presents the single-phase inverter with the 3-level, double-edge PWM scheme described by Equations (8)–(11) (so-called the first PWM scheme, presented many years ago [22]).

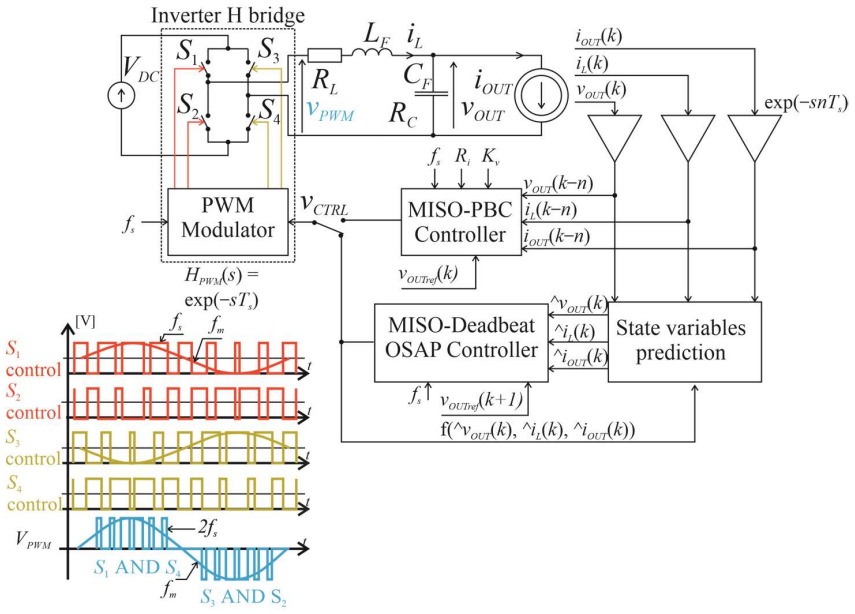


Figure 1. Single-phase 3-level H-bridge inverter with the used modulation scheme.

For $k = 1 \ldots (f_s/f_m)$:

$$S_1 : \; T_{ON}(k)/T_s = 0.5Msin(2\pi k f_m/f_s) + 0.5 \tag{8}$$

$$S_2 : \; NOT(S_1) \tag{9}$$

$$S_3 : \; T_{ON}(k)/T_s = 0.5Msin((2\pi k f_m/f_s) + \pi) + 0.5 \tag{10}$$

$$S_4 : \; NOT(S_3) \tag{11}$$

As can be seen from Figure 1, the PWM frequency is twice the switching frequency. The Bode plots of the measurement channels can be measured using the method presented in [23] and used directly for this purpose in [8]. Its general idea is to measure the ratios of the excitation signal amplitude to the fundamental signal (they are summed, and the test signal is the harmonic of the fundamental signal nf_m) at the output of the measurement channel V_{chOUT} and the same ratio at the input of the measurement channel V_{ChIN} [8]. The quotient of these two ratios gives the magnitude and phase Bode plots of the measurement channel. All the voltage and current measurement channels are the same except for the input isolation. The voltage channel has an isolated amplifier ISO 124P (Texas Instruments, Dallas, TX, USA), and the current channels include LA25 NP (LEM International SA, Meyrin, Switzerland) transducers. However, it was assigned that in the 1 kHz bandpass, they have similar frequency-based characteristics, and we measured only voltage channels. The transfer function of the measured channel is (12) for n = 1 to n_{max}. The n_{max} is the number of the highest harmonic of the fundamental frequency $f_{m,}$ used as the excitation signal (we use n_{max} = 100; however, the calculated magnitude and phase are not exact for this value).

$$K_{Ch}(\mathrm{j}2\pi \mathrm{n} f_m) = \frac{|V_{ChOUT}(nf_m)|/|V_{ChOUT}(f_m)|}{|V_{ChIN}(nf_m)|/|V_{ChIN}(f_m)|}\exp(\mathrm{j}\arg(nf_m)) \tag{12}$$

The magnitude Bode plot is (12)

$$|K_{Ch}(\mathrm{n} f_m)| = 20\log\frac{|V_{ChOUT}(nf_m)|/|V_{ChOUT}(f_m)|}{|V_{ChIN}(nf_m)|/|V_{ChIN}(f_m)|} \tag{13}$$

The phase Bode plot is (14)

$$\arg(K_{Ch}(nf_m)) = [\arg(\mathrm{V}_{ChOUT}(nf_m) - \arg(\mathrm{V}_{ChOUT}(f_m)] - [\arg(\mathrm{V}_{ChIN}(nf_m) - \arg(\mathrm{V}_{ChIN}(f_m)] \tag{14}$$

For the switching frequency f_s = 51,200 Hz (f_s is always a harmonic of the fundamental frequency f_m = 50 Hz), there are $f_s/50$ = 1024 samples of the sinusoidal reference per the fundamental period T_m = 20 ms. The minimum number of samples of the n-th harmonic in this period is equal to $f_s/(n_{max}50)$. So, for n_{max} = 100, there are about 10 samples per a fundamental period, which seems a sufficient value for further FFT calculations [15].

In [14,15], it was shown that the inductance of the inductor L_F with core made of the alloy-powder high-quality material MS-Sendust [13] has almost a constant value for the wide magnetizing current range and its frequency (the twice switching frequency). The equivalent serial resistance R_L depends on the load and switching frequency but can be approximated as equal to 1 Ω. Finally, neglecting the capacitor serial resistance, the control transfer function K_{CTRL} can be approximately presented as a product of the measurement channel transfer function K_{Ch}, the PWM modulator transfer function K_{PWM}, and the transfer function of the inverter K_{INV} (15). The relative measurement of the Bode plots means that

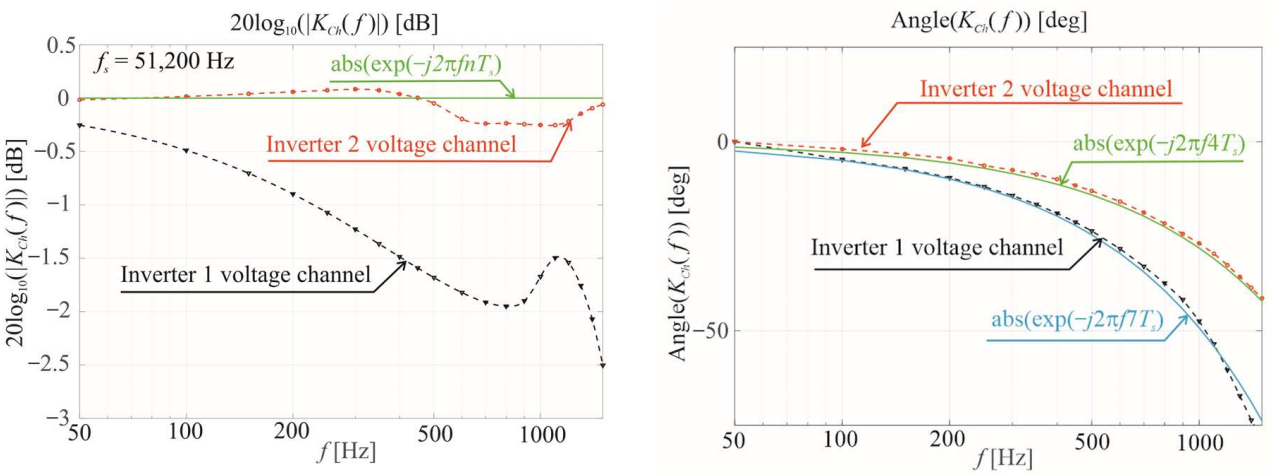
we do not measure the delay of the PWM modulator because the output fundamental waveform, treated as a reference waveform, is delayed.

$$K_{INV} \approx \frac{{\omega_{F0}}^2}{s^2 + 2\xi_F \omega_{F0} s + (1 + R_L/R_{OUT}){\omega_{F0}}^2} \tag{15}$$

$$\omega_{F0} \approx \frac{1}{\sqrt{L_F C_F}}$$

$$\xi_{F0} \approx \frac{1}{2}\frac{1}{\omega_{F0}}\left(\frac{1}{C_F R_{OUT}} + \frac{R_L}{L_F}\right)$$

Figure 2 presents the Bode plots of two experimental inverter models. The measured delays of channels include the zero-order-hold function of the analog-to-digital converters but do not include the PWM modulator delay.



(**a**) (**b**)

Figure 2. The Bode plots of the output voltage measuring channels of two experimental inverter models, (**a**) Bode magnitude plot, (**b**) Bode phase plot.

It was shown in [8] that for the high switching frequency (about 50 kHz), we can omit the prediction of the state variables in some types of controllers (e.g., PBC).

3. The Discrete Model of the Single-Phase Inverter with the 3-Level Double-Edge PWM

The controlled object should be described with the state equations where the state–space variables are $\mathbf{x} = [v_{OUT}\ i_{LF}\ i_{OUT}]^{\mathrm{T}}$, input variable $\mathbf{u} = v_{FIN}$ − the envelope of v_{PWM} (Figure 1), and output variable $\mathbf{y} = v_{OUT}$, the state–space equations (for $R_C = 0$) are (16) and (17).

$$\dot{\boldsymbol{x}} = \boldsymbol{A}\boldsymbol{x} + \boldsymbol{B}\boldsymbol{u},\ \boldsymbol{y} = \boldsymbol{C}\boldsymbol{x} \tag{16}$$

$$\boldsymbol{A} = \begin{bmatrix} 0 & \frac{1}{C_F} & -\frac{1}{C_F} \\ -\frac{1}{L_F} & -\frac{R_L}{C_F} & 0 \\ 0 & 0 & 0 \end{bmatrix},\ \boldsymbol{B} = \begin{bmatrix} 0 \\ \frac{1}{L_F} \\ 0 \end{bmatrix},\ \boldsymbol{C} = \begin{bmatrix} 1 & 0 & 0 \end{bmatrix} \tag{17}$$

The state–space Equation (16) is solved in the switching period [1,24]. The obtained exponential function of T_{ON} time for the double-edge modulation depends on the PWM modulation type and is approximated using simple linearization (18).

$$e^{\boldsymbol{A}T_{ONk}/2} \approx \boldsymbol{I} + \boldsymbol{A}T_{ONk}/2 \tag{18}$$

The linearized discrete state–space equations [11] are (19) and (20), where v_{CTRL} is the input signal of the PWM modulator (Figure 1).

$$\boldsymbol{x}(k+1) = \boldsymbol{A}_D\boldsymbol{x}(k) + \boldsymbol{G}_D T_{ON}(k) = \boldsymbol{A}_D\boldsymbol{x}(k) + \boldsymbol{G}_D \frac{T_s}{V_{DC}} v_{CTRL}(k) \tag{19}$$

$$\boldsymbol{y}(k+1) = \boldsymbol{C}_D\boldsymbol{x}(k) \tag{20}$$

The state, input, and output matrices are (21)

$$\boldsymbol{A}_D = \boldsymbol{\Phi}(T_s) = \begin{bmatrix} \phi_{11} & \phi_{12} & \phi_{13} \\ \phi_{21} & \phi_{22} & \phi_{23} \\ \phi_{31} & \phi_{32} & \phi_{33} \end{bmatrix}, \ \boldsymbol{G}_D = \begin{bmatrix} g_{11} \\ g_{21} \\ g_{31} \end{bmatrix}, \ \boldsymbol{C}_D = \boldsymbol{C} \tag{21}$$

In the presented approach, the load current is treated as an independent state variable. It is illustrated in Figure 1, where the load current is presented as the current source. So the damping factor (22) is different from (15). We lose the dependence between output voltage and the output current, but it is a widely presented approach [25–30].

$$\xi_F = \frac{1}{2} R_L \sqrt{\frac{C_F}{L_F}}, \ \omega_{F0} = \frac{1}{\sqrt{C_F L_F}}, \ E_A = exp(-\xi_F \omega_{F0} T_s), \ E_G = sqrt(-\xi_F \omega_{F0} T_s/2) \tag{22}$$

Coefficients of state matrix:

$$\varphi_{11} = [cos(\omega_{F0} T_s) + \xi_F sin(\omega_{F0} T_s)] E_A, \ \varphi_{12} = \frac{1}{\omega_{F0} C_F} sin(\omega_{F0} T_s) E_A \tag{23}$$

$$\varphi_{13} = -\varphi_{12} + R_L(\varphi_{11} - 1),$$

$$\varphi_{21} = -\frac{C_F}{L_F}\varphi_{12}, \ \varphi_{22} = [cos(\omega_{F0} T_s) - \xi_F sin(\omega_{F0} T_s)] E_A, \ \varphi_{23} = 1 - \varphi_{11},$$

$$\varphi_{31} = 0, \ \phi_{32} = 0, \ \ \varphi_{33} = 1$$

Coefficients of input matrix:

$$g_{11} = V_{DC} \omega_{F0} sin(\omega_{F0} T_s/2) E_G, \tag{24}$$

$$g_{21} = \frac{V_{DC}}{L_F} [cos(\omega_{F0} T_s/2) - \xi_F sin(\omega_{F0} T_s/2)] E_G, \ g_{31} = 0$$

4. The Simulation of the Inverter with the Pure Discrete One-Sample-Ahead Preview Controller—MISO Deadbeat

The deadbeat control [1–3,21,31,32] applies feedback of the inverter that sets all poles of the closed-loop transfer function to the origin of the z-plane. The basic deadbeat approach is for linear systems. Deadbeat control brings the output to the steady state in the smallest number of time steps. For an n-th-order linear system, it can be shown that the minimum number of steps will be n. It means that in the inverter, we can obtain the reference value of the output voltage in the $k + 1$ switching period. It was described by A. Kawamura [1] many years ago in 1988 as one-sample-ahead preview control (OSAP). OSAP was also presented in the newer papers [2,3]. A. Kawamura [1] showed that assuming v_{OUT} $(k + 1) = v_{ref}$ $(k + 1)$ leads to a deadbeat control law. Deadbeat control law does not require setting gains of the voltage or current. It depends on the parameters of the control system, and that is why it is very sensitive to their values. SISO deadbeat control is also very sensitive to delays in the plant open-loop transfer function [33]. If the plant-inverter with the double-edge PWM [11]

has the (25) K_{OPEN_LOOP} control function, where z^{-d} delay is included, the (26) deadbeat controller G_R transfer function should be used, and the (27) difference control law.

$$K_{OPEN_LOOP} = \frac{v_{OUT}(z^{-1})}{v_{CTRL}(z^{-1})} = z^{-d}\frac{b_1 z^{-1} + b_2 z^{-2}}{1 + a_1 z^{-1} + a_2 z^{-2}} \tag{25}$$

$$G_R = \frac{v_{CTRL}(z^{-1})}{v_{ref}(z^{-1}) - v_{OUT}(z^{-1})} = \frac{\frac{1}{b_1 + b_2}(1 + a_1 z^{-1} + a_2 z^{-2})}{1 - \frac{1}{b_1 + b_2}(b_1 z^{-1} + b_2 z^{-2})z^{-d}} \tag{26}$$

$$\begin{aligned} v_{CTRL}(k) = {} & (v_{ref}(k) - v_{OUT}(k))\tfrac{1}{b_1+b_2} + (v_{ref}(k-1) - v_{OUT}(k-1))\tfrac{a_1}{b_1+b_2} \\ & + (v_{OUT}(k-2) - v_{ref}(k-2))\tfrac{a_2}{b_1+b_2} + v_{CTRL}(k-1 \\ & - d)\tfrac{b_1}{b_1+b_2} + v_{CTRL}(k-2-d)\tfrac{b_2}{b_1+b_2} \end{aligned} \tag{27}$$

where

$$a_1 = -(\varphi_{11} + \varphi_{22}),$$

$$a_2 = \varphi_{11}\varphi_{22} - \varphi_{12}\varphi_{21},$$

$$b_1 = \frac{T_c}{V_{DC}} g_{11},$$

$$b_2 = \frac{T_c}{V_{DC}}(\varphi_{11}\varphi_{22} - \varphi_{12}\varphi_{21}),$$

$d \geq 1$—depends on the delay of the output voltage measurement channel.

The SISO deadbeat control in inverters is rather useless. However, MISO-OSAP deadbeat control with measuring output voltage, inductor current, and output current, owing to control of these values that are dependent on the filter parameters, is much more useful.

From (19) to (24), we can write Equation (28).

$$v_{OUT}(k+1) = \varphi_{11} v_{OUT}(k) + \varphi_{12} i_{LF}(k) + \varphi_{13} i_{OUT}(k) + g_{11}\frac{T_s}{V_{DC}} v_{CTRL}(k) \tag{28}$$

If we assume $v_{OUT}(k+1) = v_{ref}(k+1)$ we receive MISO-OSAP control (29).

$$v_{CTRL}(k) = \frac{1}{g_{11}}\frac{V_{DC}}{T_s}[v_{ref}(k+1) - \varphi_{11} v_{OUT}(k) - \varphi_{12} i_{LF}(k) - \varphi_{13} i_{OUT}(k)] \tag{29}$$

The value of V_{DC} simplifies into Equation (29) with the value of V_{DC} in g_{11} from Equation (24), so it is possible to assume V_{DC} = 1.

The prediction of the delayed measured variables is the approach that enables the usage of the deadbeat control in inverters, e.g., based on the idea of a fractional-order Smith Predictor [34]. In [35], the combination of deadbeat PI control and the Smith method was proposed as a fast and stable current control method that can achieve deadbeat characteristics even in the presence of delays. In [36], a digital extended state observer improves the robustness of the parameter variations and the delay variation of the system with deadbeat control. In [37], the problem of the delay is solved using state observers. The full-order state Luenberger observer seems a reasonable solution for the 3-input state variables prediction in the system with delays with MISO-OSAP deadbeat controller [4,5,37]. The Luenberger observer or other similar linear observers are often used in inverters' control systems [38–42]. The description of the Luenberger observer in a case when we measure all the state variables and we want to predict them is found in Equations (30) and (31). The

matrix C_L (30) is different from the C_D (17) because now all the state variables are in the output of the Luenberger observer.

$$\mathbf{y} = \mathbf{x},\ \mathbf{C_L} = \begin{bmatrix} 1 & 0 & 0 \\ 0 & 1 & 0 \\ 0 & 0 & 1 \end{bmatrix} \tag{30}$$

$$\hat{\boldsymbol{x}}(k+1) = \boldsymbol{A}_D\hat{\boldsymbol{x}}(k) + \boldsymbol{G}_D T_{ON}(k) + \boldsymbol{L}[\boldsymbol{y}(k) - \boldsymbol{C}_L\hat{\boldsymbol{x}}(k)] \tag{31}$$

The error of the system (31) is described by Equation (32).

$$\boldsymbol{e}(k+1) = (\boldsymbol{A}_D - \boldsymbol{L}\boldsymbol{C}_L)[\boldsymbol{x}(k) - \hat{\boldsymbol{x}}(k)] = (\boldsymbol{A}_D - \boldsymbol{L}\boldsymbol{C}_L)\boldsymbol{e}(k) \tag{32}$$

The matrix of Luenberger observer gains for three state variables [v_{OUT}, i_{LF}, i_{OUT}] is (33).

$$\boldsymbol{L} = \begin{bmatrix} l_{\mathrm{vOUT}} & 0 & 0 \\ 0 & l_{\mathrm{iLF}} & 0 \\ 0 & 0 & l_{\mathrm{iOUT}} \end{bmatrix} \tag{33}$$

The characteristic equation of the full-state Luenberger observer is (34).

$$det\left(z\begin{bmatrix} 1 & 0 & 0 \\ 0 & 1 & 0 \\ 0 & 0 & 1 \end{bmatrix} - \boldsymbol{A}_D + \boldsymbol{L}\boldsymbol{C}_L\right) = 0 \tag{34}$$

Equation (34) in the case of 3 state variables is equal to (35), (36).

$$det\begin{bmatrix} z - \varphi_{11} + l_1 & -\varphi_{12} & -\varphi_{13} \\ -\varphi_{21} & z - \varphi_{22} + l_2 & -\varphi_{23} \\ 0 & 0 & z - 1 + l_3 \end{bmatrix} = 0 \tag{35}$$

$$(z - 1 + l_3)[(z - \varphi_{11} + l_1)(z - \varphi_{22} + l_2) - \varphi_{12}\varphi_{21}] = 0 \tag{36}$$

The roots of the characteristic equation of the Luenberger observer (41) are independent of the closed feedback-loop control system according to the "separation theorem" [43]. The observer eigenvalues should allow faster convergence to zero of the observation error than the transient process in a closed-loop system, which will happen if the roots of their characteristic Equation (31) are closer to zero on the z-plane (their absolute value is lower) than the roots of the characteristic equation of the closed-loop system without prediction. This is not possible in the case of the deadbeat control when all the poles of the closed-loop system are zeroes. The different versions of the linear observers, such as the Luenberger observer, have different algorithms for calculating the value of the observer characteristic equation roots vs. the closed-loop system characteristic equation roots. In [43], the Luenberger observer was designed with its dynamics three times faster than the fastest pole of the plant. In the case of deadbeat control, where closed-loop poles are at the origin of the z-plane, there is no simple algorithm for setting the Luenberger gains inside the allowable range. If we assign [43] the pole position of the state observer [44], we can call the acker() function in MATLAB R2021b to obtain the feedback gain matrix of the state observer. In [45] there is assigned for the continuous system the proportionality coefficient between eigenvalues of the object λ_m and observer λ_e (λ_e = k λ_m, k > 1) and finally, the observer gains are calculated. In [46], it is written that the observer gain matrix should be chosen so that all eigenvalues of the continuous version of (32) have real negative parts. It is the same approach as keeping the roots of the characteristic equation of the discrete

state observer inside the unit circle in the z-plane. The positive values of observer gains are assigned. The values of l_{vOUT}, l_{iLF}, and l_{iOUT} are set experimentally so that the system (31) is stable and sufficiently fast. The different sets of observer gains give different results (the output voltage distortions) for the different delays (Table 1). All three roots z_i of (35), (36) should be inside the unit circle in the z-plane (37).

$$|z_i| < 1 \tag{37}$$

Table 1. Output voltage distortions in simulations of the MISO-OSAP control without and with Luenberger observer and MISO-PBC control, for the rectifier RC load (PF ≈ 0.7) and different additional delay d.

Controller Type	THD [%] $d = 0$	THD [%] $d = T_s$	THD [%] $d = 2T_s$	THD [%] $d = 3T_s$	THD [%] $d = 4T_s$	THD [%] $d = 5T_s$	THD [%] $d = 6T_s$	THD [%] $d = 7T_s$
MISO-OSAP (M = 0.2)	0.2656	Osc.	Osc.	Osc.	Osc.	Osc.	Osc.	Osc.
MISO-OSAP (M= 0.7)	0.5782	Osc.	Osc.	Osc.	Osc.	Osc.	Osc.	Osc.
MISO-OSAP-LO (M = 0.7, l_1 = 0.25, l_2 = 0.01, l_3 = 1)	0.2415	0.3478	0.4712	0.5723	1.056	0.8301	6.85	Osc.
MISO-OSAP-LO (M = 0.7, l_1 = 0.15, l_2 = 0.01, l_3 = 1)	0.3764	0.4192	0.6352	1.102	1.006	1.207	1.440	1.830
MISO-PBC (M = 0.7, K_v = 0.3, R_i = 20)	0.1773	0.201	0.276	0.3445	7.827	Osc.	Osc.	Osc.
MISO-PBC (M = 0.7, K_v = 0.2, R_i = 10)	0.2124	0.315	0.439	0.5905	0.7362	0.9022	1.292	Osc.

So

$$z_1 = 1 - l_{iOUT} \tag{38}$$

We should solve the following Equation (39) to find z_2 and z_3.

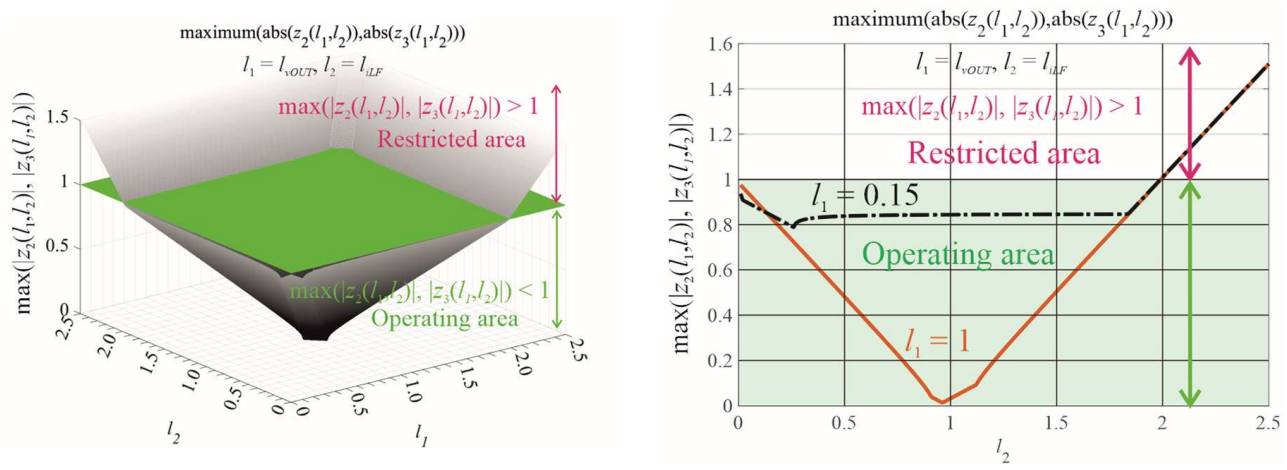
$$z^2 + z(l_{vOUT} + l_{iLF} - \varphi_{11} - \varphi_{22}) + (l_{vOUT}l_{iLF} - \varphi_{22}l_{vOUT} - \varphi_{11}l_{iLF} + \varphi_{11}\varphi_{22} - \varphi_{12}\varphi_{21}) = 0 \tag{39}$$

The roots z_2 and z_3 are calculated as (40)

$$z_{2,3} = \left[\pm\sqrt{[(l_{vOUT} - l_{iLF}) + (\varphi_{22} - \varphi_{11})]^2 + 4\varphi_{12}\varphi_{21}} - (l_{vOUT} + l_{iLF} - \varphi_{11} - \varphi_{22})\right]/2 \tag{40}$$

Figure 3a presents the area in which maximum ($|z_2(l_{vOUT}, l_{iLF})|$ $|z_3(l_{vOUT}, l_{iLF})|$) < 1 (below green plane) for f_s = 51.2 kHz, L_F = 2 mH, C_F = 51 µF. The final approximated restriction is for l_{vOUT}, l_{iLF}, l_{iOUT} > 0: l_{vOUT} < 2, l_{iLF} < 2, l_{iOUT} < 2. However, the position of z_i varies in these allowable ranges of l_i values. It is shown in Figure 3b (it is a cross-section of Figure 3a). The lowest value of $|z_1|$, $|z_2|$, and $|z_3|$, so the fastest Luenberger observer is for $l_{vOUT} \approx 1$, $l_{iLF} \approx 1$, $l_{iOUT} \approx 1$. Finally, the gains of the Luenberger observer should be adjusted in the allowable area (Figure 3b) for the particular inverter design.

Figure 4 presents the MATLAB/Simulink scheme of the VSI with only ZOH (analog-to-digital converter ADC) and PWM modulator delays.



(**a**) (**b**)

Figure 3. (**a**) The allowable area of $l_1 = l_{vOUT}$ and $l_2 = l_{iLF}$ values below the green plane for f_s = 51,200 Hz, L_F = 2 mH, C_F = 51 µF; (**b**) the cross-sections of Figure 3a for $l_{vOUT} \approx 0.15$ and $l_{vOUT} \approx 1$.

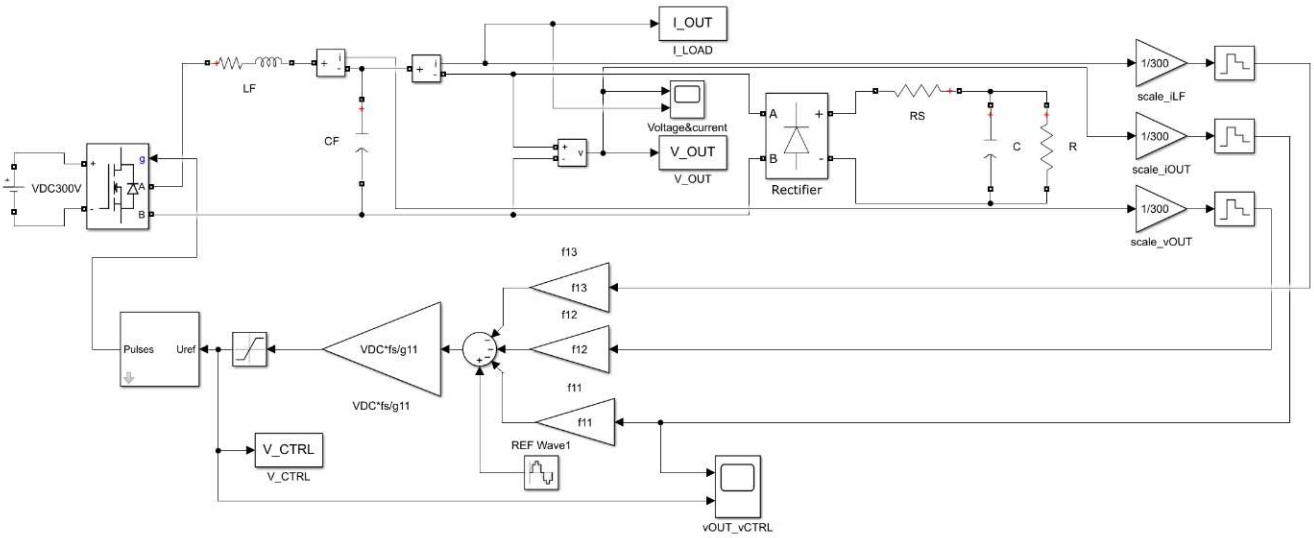


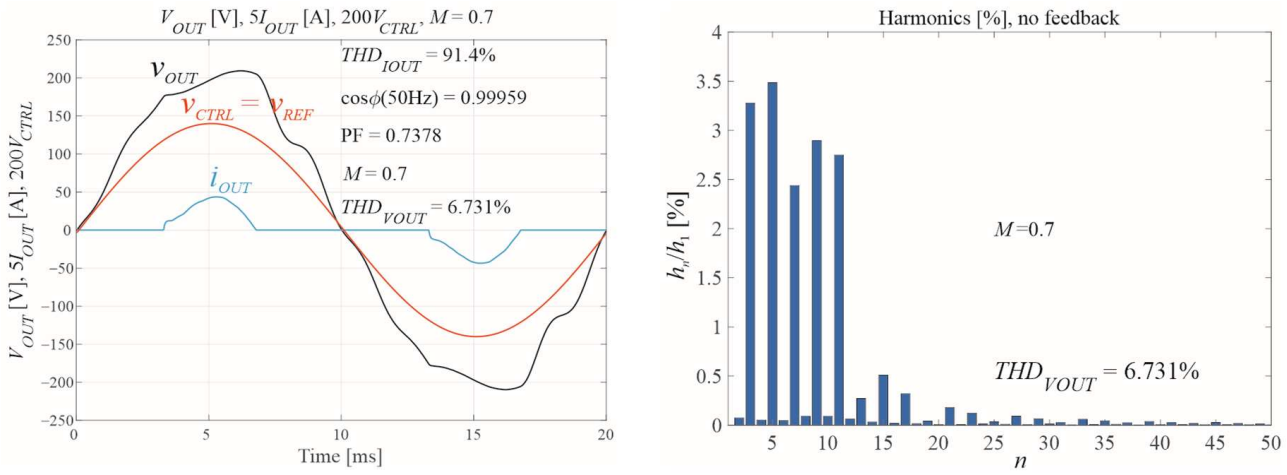
Figure 4. The VSI without additional delays in the measurement channels (except ADC and PWM) and MISO-OSAP-deadbeat control.

The voltage and current waveforms and harmonics for the VSI without feedback are shown in Figure 5. The modulation index M = 0.7 was assigned. All the inverter and the rectifier RC load parameters are as previously described.

Implementing MISO-OSAP-deadbeat control seriously reduces the THD of the output voltage, as shown in Figure 6. However, only ADC (simulated by ZOH module) and PWM modulator delays are present. The modulation index M = 0.7 was assigned.

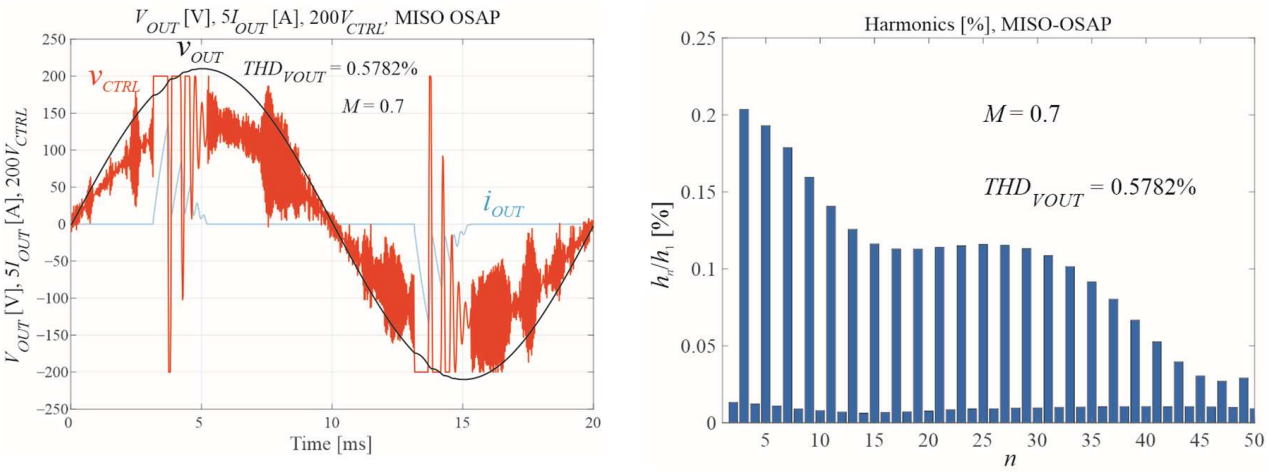
It can be seen that the MISO-OSAP controller is very fast and efficiently reduces output voltage distortions. However, for M = 0.7, the PWM modulator is saturated (the control voltage exceeds the upper input modulator limits equal to ±1 in simulation). So the simulation was repeated for the highest modulation index M = 0.2 for which the control voltage does not exceed the input limits of the PWM modulator (±1). The low modulation

index M = 0.2 will never be used in practice, but Figure 7 presents the top capabilities of the MISO-OSAP control in the system with low delays. In all the next presented simulations, the M = 0.7, even if it leads to a small saturation of the modulator. In the experimental VSI for the STM32V407G microprocessor control (84 MHz in the input of the PWM modulator) and f_s = 51,200 Hz, the PWM modulator limits are ±820 units (it is adequate to ±1 in simulation).



(**a**) (**b**)

Figure 5. (**a**) Simulation of the output voltage, output current and control voltage (equal to reference voltage) waveforms for VSI without the feedback; (**b**) the harmonics of the output voltage for the VSI without feedback for the rectifier RC load (f_s = 51,200 Hz, L_F = 2 mH, C_F = 51 µF, R_L = 1 Ω R_s = 1 Ω, C = 40 µF, R = 100 Ω, M = 0.7, PF ≈ 0.7).

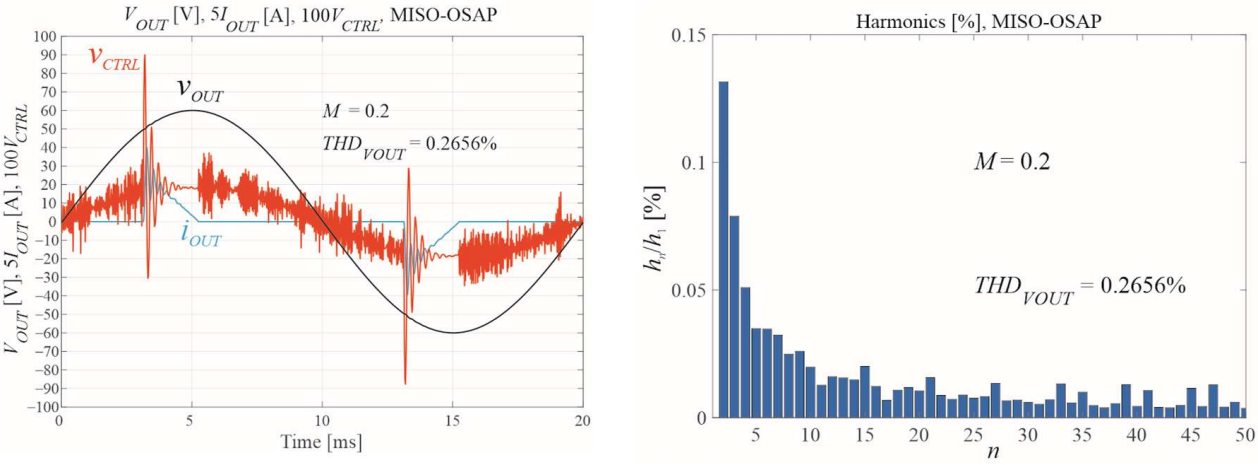


(**a**) (**b**)

Figure 6. (**a**) Simulation of the output voltage, output current and control voltage waveforms for VSI with the MISO-OSAP control (without the additional delay in the measurement channels); (**b**) the harmonics of the output voltage for the rectifier RC load for M = 0.7 (f_s = 51,200 Hz, L_F = 2 mH, C_F = 51 µF, R_L = 1 Ω R_s = 1 Ω, C = 430 µF, R = 100 Ω, M = 0.7, PF ≈ 0.7).

The additional delays in the measurement channels cause oscillations of the output voltage for the MISO-OSAP control. The proposed solution is the prediction of the measured and delayed state variables. The previously presented full-order state Luenberger observer (31) will be implemented in the control loop. Figure 8 presents the MATLAB/Simulink scheme of the VSI with delays (here, there are delays of the ZOH-ADC units, PWM

modulator, and additional up to $5T_s$ in each measurement channel). In this particular case of the VSI parameters, the Luenberger observer gains were experimentally appointed (in the allowable ranges) to obtain the lowest distortions for the reasonable delay ($5T_s$) (l_1 = 0.15 or 0.25, l_2 = 0.01, l_3 = 1). Figure 9 presents a simulation of the output voltage, output current, and control voltage waveforms for the VSI with the MISO-OSAP-LO control for the rectifier RC load for M = 0.7 and an additional delay of $5T_s$. For additional delays over $7T_s$, the distortions of the output voltage increase (Table 1). Two different sets of observer gains are assigned for different delays (Table 1).



(**a**) (**b**)

Figure 7. (**a**) Simulation of the output voltage, output current and control voltage waveforms for VSI with the MISO-OSAP control (without the additional delay in the measurement channels); (**b**) the harmonics of the output voltage for the rectifier RC load for M = 0.2 when PWM modulator is not saturated (f_s = 51,200 Hz, L_F = 2 mH, C_F = 51 µF, R_L = 1 Ω R_s = 1 Ω, C = 430 µF, R = 100 Ω, M = 0.2, PF ≈ 0.7).

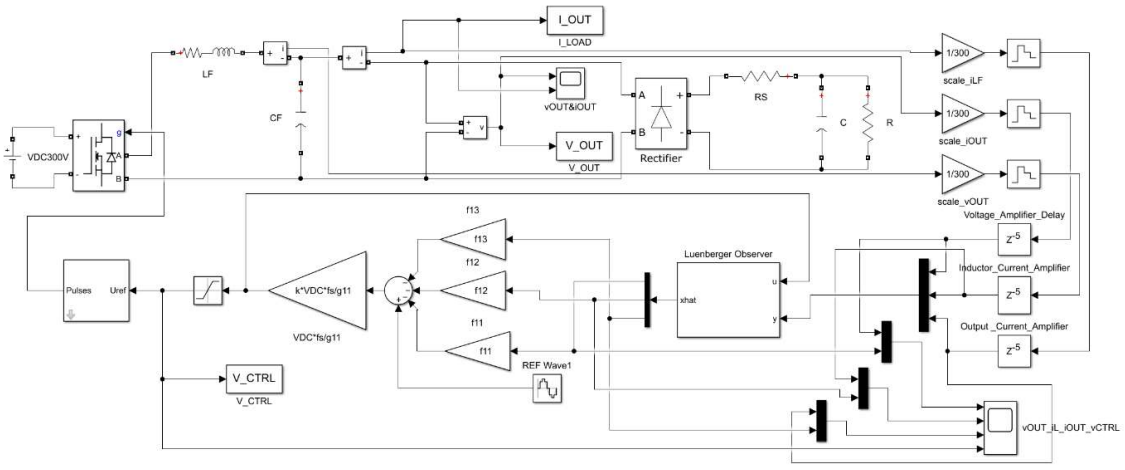
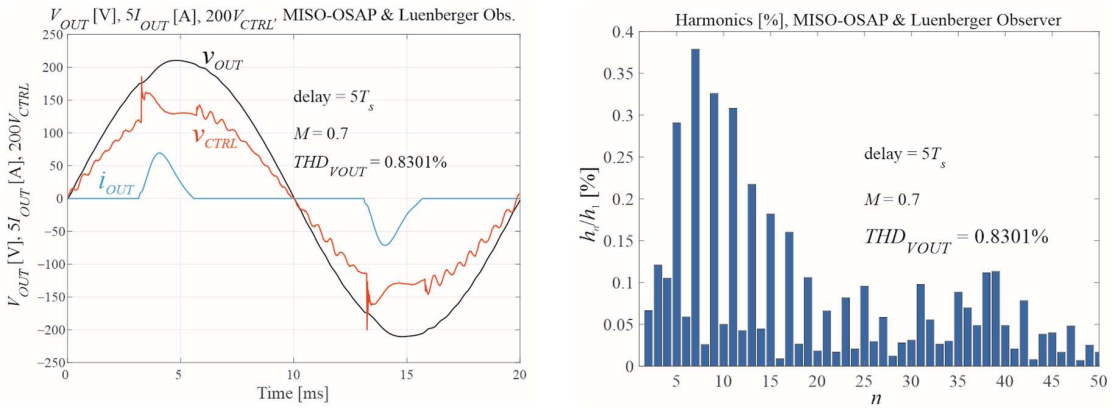


Figure 8. The VSI with the exemplary additional delays $5T_s$ in the measurement channels (with basic ADC and PWM modulator delays) and MISO-OSAP deadbeat control with full-order state Luenberger observer (MISO-OSAP-LO).



(**a**) (**b**)

Figure 9. (**a**) Simulation of the output voltage, output current and control voltage waveforms for VSI with the MISO-OSAP-LO control; (**b**) the harmonics of the output voltage for the rectifier RC load for M = 0.7 for additional delay $5T_s$ (f_s = 51,200 Hz, L_F = 2 mH, C_F = 51 µF, R_L = 1 Ω R_s = 1 Ω, C = 430 µF, R = 100 Ω, M = 0.2, PF ≈ 0.7, l_1 = 0.25, l_2 = 0.01, l_3 = 1).

5. The Simulation of the Inverter with the Discretized Version of MISO Passivity-Based Control

This section aims to compare the pure discrete MISO-OSAP described in Section 4 with the efficient discretized MISO control. The passivity-based control (PBC) [6,25,47–53], which considers the energy stored in the system (Hamiltonian function (41), similar to Lyapunov function [47]), was chosen. The idea of PBC is that the energy stored in the VSI system, in the filter inductor, and the filter capacitor (41), should be lower than the energy delivered to the system.

$$H(x) = \frac{1}{2}\left(L_F {i_{LF}}^2 + C_F {v_{OUT}}^2\right) \tag{41}$$

The PBC is based on "injecting" the virtual "resistance" R_i (R_i is the current gain) into the system. In the improved PBC [25,47], the output voltage error is directly implemented in the control law (the voltage gain is K_v). The discretized control laws of PBC, according to Figure 1, where we consider predicted state variables, are Equations (42) and (43) [8].

$$v_{CTRL}(k) = -R_i i_{LF}(k) + (R_i + R_L) i_{LFref}(k) + L_F \frac{i_{LFref}(k) - i_{LFref}(k-1)}{T_s} + v_{REF}(k) \tag{42}$$

$$i_{LFref}(k) = K_v[v_{REF}(k) - v_{OUT}(k)] + C_F \frac{v_{REF}(k) - v_{REF}(k-1)}{T_s} + i_{OUT}(k) \tag{43}$$

For $R_L + R_i > 0$ (R_L is always > 0 and we assign that $R_i > 0$) and $K_v > 0$, the roots of the characteristic equation of the closed-loop system with PBC are always in the left half s-plane, the system is stable [6]. The 3-level modulation PWM modulator has a limited output voltage increase speed: V_{DC}/T_s. The increase of the control voltage from (42) cannot be faster than (44) [54].

$$\left|\frac{dv_{CTRL}(kT_s)}{dt}\right| \leq \frac{V_{DC}}{T_s} \tag{44}$$

For the worst case of the inverter load $R_{LOAD} = \infty$, for the system without delays, Equation (44) using (42) and (43) can be presented as (45).

$$K_v[L_F + (R_i + R_L)T_s]\frac{1}{L_F C_F} + \frac{R_i}{L_F} < f_s \tag{45}$$

The product $R_i K_v$ is restricted depending on the switching frequency f_s. The convergence of error is faster for the higher values of K_v and R_i gains. The high values of the gains cause saturation of the PWM modulator, leading to the output voltage oscillations. The PBC control results in a lower THD of the output voltage for the higher switching frequency, allowing for higher current and voltage gains. Figure 10 presents the admissible operating areas of PBC as a function of gains R_i, K_v for f_s = 51,200 Hz and three values of R_L (0.5, 1.0, and 1.5 Ω). It can be seen that the serial equivalent resistance does not noticeably influence the admissible gains area. The presented relation (44) is approximated, and the final fine adjustments should be done experimentally. Figure 11 presents the MATLAB/Simulink scheme of VSI with MISO-PBC control. Figure 12 shows the output voltage, output current, and control voltage waveforms for the VSI with the MISO-PBC control without additional delay in the measurement channels. The output voltage harmonics for the experimentally appointed gains are K_v = 0.3 and R_i = 20. Figure 13 shows the same waveforms but for the additional delay $5T_s$ in the measurement channels for the lower gains K_v = 0.2 and R_i = 10, because for K_v = 0.3 and R_i = 20, there were oscillations of the output voltage. The results of the simulations for the different additional delays in the measurement channels are presented in Table 1.

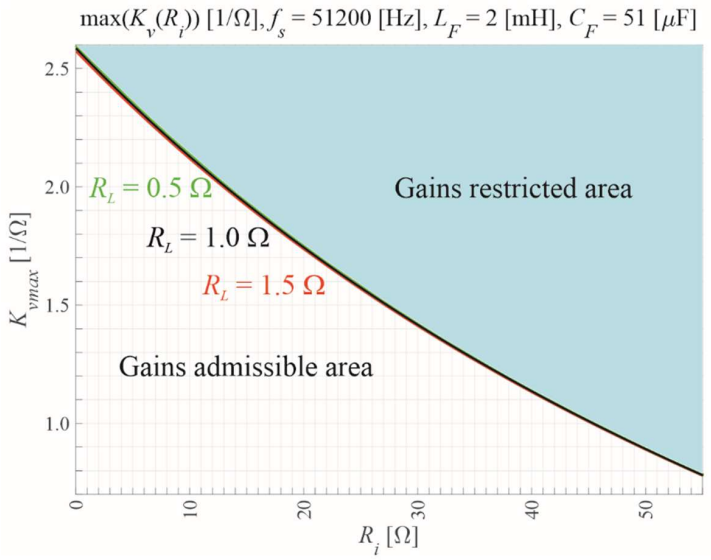


Figure 10. The operating areas of PBC as a function of gains R_i, K_v for f_s = 51.2 kHz and three values of R_L (0.5, 1.0, and 1.5 Ω).

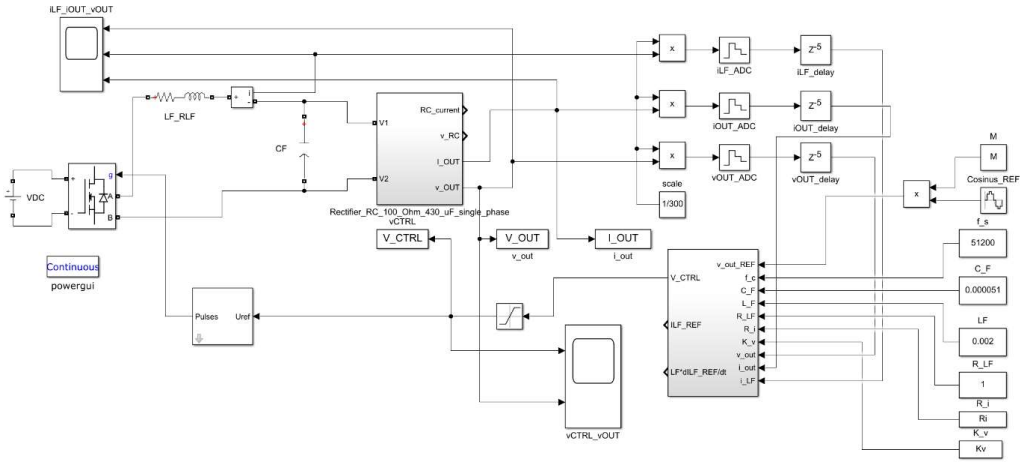
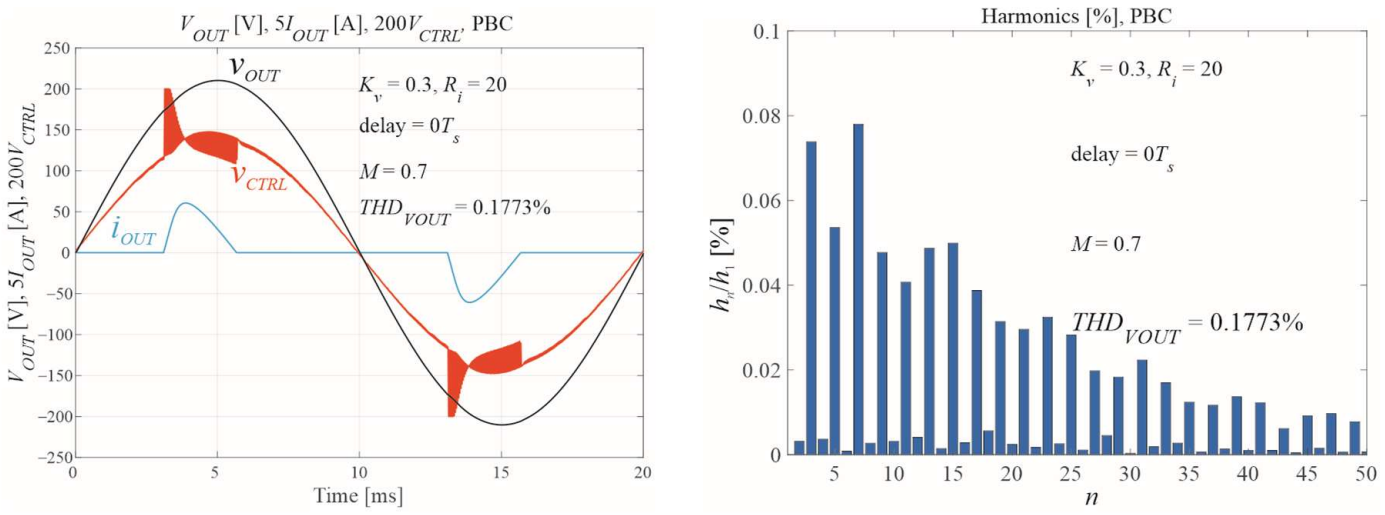
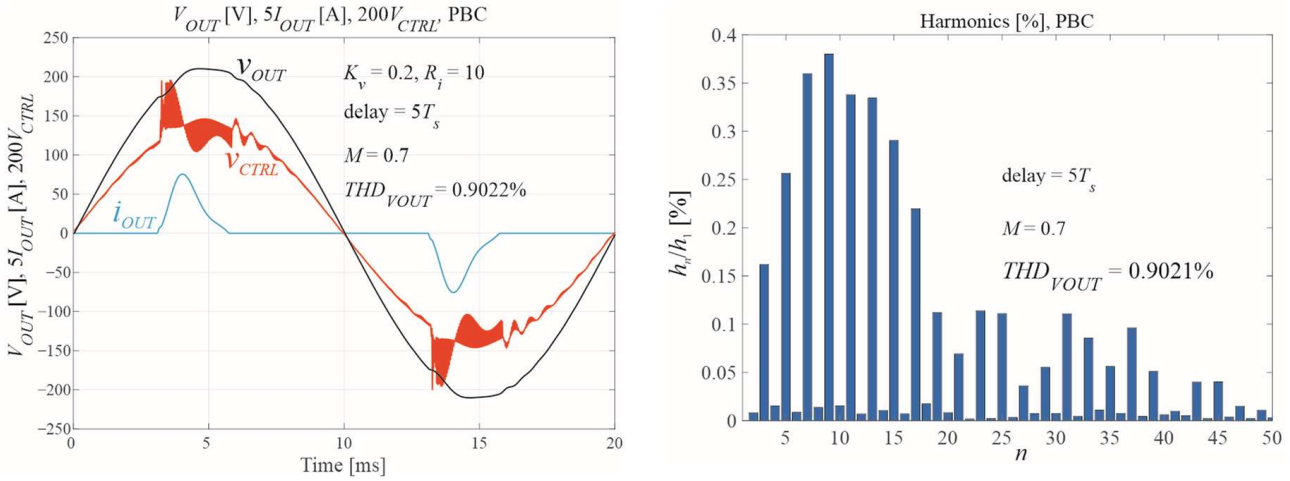


Figure 11. Matlab/Simulink scheme of VSI with the MISO-PBC control modeled with exemplary delays.



(**a**) (**b**)

Figure 12. (**a**) Simulation of the output voltage, output current and control voltage waveforms for VSI with the MISO-PBC control; (**b**) the harmonics of the output voltage for the rectifier RC load for $M = 0.7$ without additional delay (f_s = 51,200 Hz, L_F = 2 mH, C_F = 51 µF, R_L = 1 Ω, R_s = 1 Ω, C = 430 µF, R = 100 Ω, M = 0.2, PF ≈ 0.7, K_v = 0.3, R_i = 20).



(**a**) (**b**)

Figure 13. (**a**) Simulation of the output voltage, output current and control voltage waveforms for VSI with the MISO-PBC control; (**b**) the harmonics of the output voltage for the rectifier RC load for $M = 0.7$ with additional delay $5T_s$ (f_s = 51,200 Hz, L_F = 2 mH, C_F = 51 µF, R_L = 1 Ω R_s = 1 Ω, C = 430 µF, R = 100 Ω, M = 0.2, PF ≈ 0.7, K_v = 0.2, R_i = 10).

6. The Discussion of the Simulation Results

The delay in the measurement channel is a sum of the ADC delay (it is modeled as a ZOH unit) and the additional delay in the channel presented in Figure 2. The PWM modulator implements the delay equal to T_s. Table 1 shows that for the low delay in the measurement channel, the results of the control with MISO-OSAP with Luenberger observer (MISO-OSAP-LO) and MISO-PBC control are similar. It was assumed that for THD up to about 1.5%, the results are only negligibly different. PBC does not need any variable prediction for the relatively high switching frequency f_s = 51,200 Hz. In both cases, there are admissible ranges of the gains of the LO and the PBC. These LO gains should be adjusted and should be lower for the higher delay. Such a limit, in the case of

MISO-OSAP-LO and MISO-PBC, is the additional delay of $6T_s$, together with the analog-to-digital conversion of about $7T_s$ (Table 1). MISO-OSAP without LO in case of lack of the additional delay is so fast that to obtain its best properties, we should use a very low, unimportant in practice modulation index M = 0.2 (Figure 7, Table 1). Looking at the simulation results in Table 1, we would rather choose MISO-PBC control. The parameter of VSI that can be changed is the equivalent serial resistance R_{LF}. We design the controller for R_L = 1 Ω. For the delay $5T_s$, the MISO-OSAP-LO designed (l_1 = 0.25, l_2 = 0.01, l_3 = 1) for R_L = 1 Ω, while R_L = 0.5/1/1.5 Ω has THD of the output voltage: 1.32%/0.83%/0.68%. So, the MISO-OSAP-LO is practically robust to the variable equivalent resistance. In both cases, the gains of the Luenberger observer or the PBC gains should be adjusted. So, the advantage of MISO-OSAP control, of not requiring any adjustment, disappears.

7. The Test of the Experimental Models of Inverters with OSAP and PBC Controls

The easiest way to experimentally verify the previous simulations is to use the real-time interface (MicroLabBox—RTI 1202) that has an FPGA programmed with the compiled simulation scheme from MATLAB/Simulink 2021b with dSpace Release 2021-B libraries. In simulation, scaling all the measured state variables was very simple—we just divided all the measured values by the DC voltage value because the reference voltage was a sinusoidal waveform with a unity amplitude multiplied by the modulation index M. In the case of RTI, we should set the gain factor in the voltage measurement channel for the open loop, the nominal output voltage, and a nominal load of 50 Ω to obtain the dSpace reference voltage range (amplitude $\pm 0.5M$, in Figure 4 equal to ± 0.4 for M = 0.8). We set all the voltage and current gains in the dSpace ControlDesk 7.5 (Figure 14) for the assigned input DC voltage V_{DC} and the modulation index M. The gain in the output current measuring channel should be set to the reference range, and in the controller input divided by the referenced load resistance—50 (Figures 15 and 16). A similar procedure should be performed with the inductor current measurement channel. In the case of the scaling of the inductor current, it is a sum of the output current and the filter capacitor current. So, for the fundamental frequency of 50 Hz, the load resistance of 50 Ω, and the output filter capacitor of 51 μF, we should divide the inductor current measurement by 27.76.

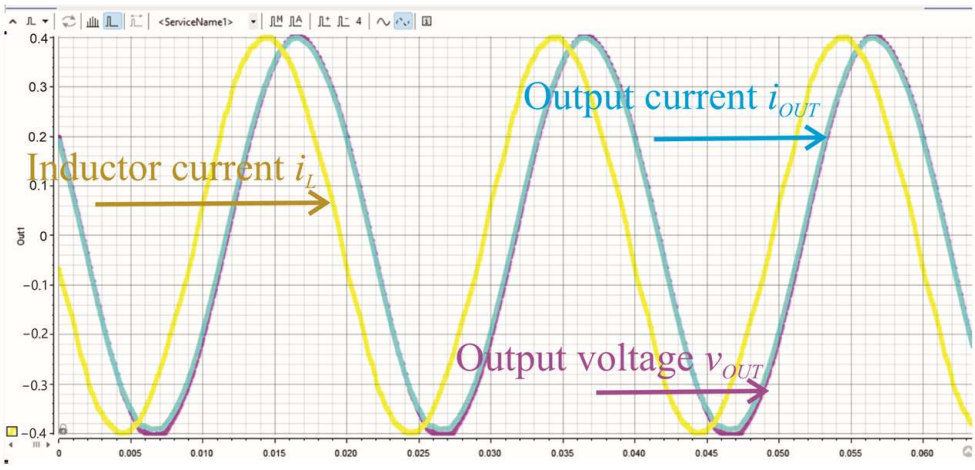


Figure 14. Adjustment of voltage and current gains in dSpace ControlDesk 7.5 for V_{REF} amplitude ± 0.4 (output voltage: v_{OUT}, output current: i_{OUT}, inductor current: i_L).

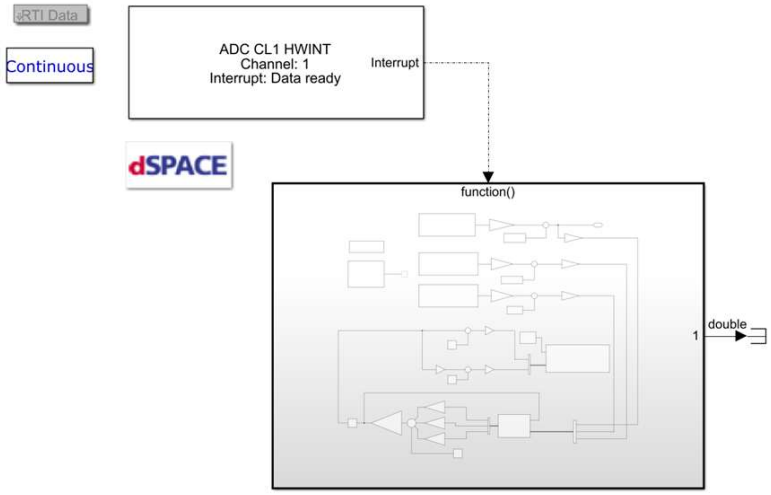


Figure 15. The idea of the function block called by the ADC Channel 1 interrupt (data ready for measuring the output voltage).

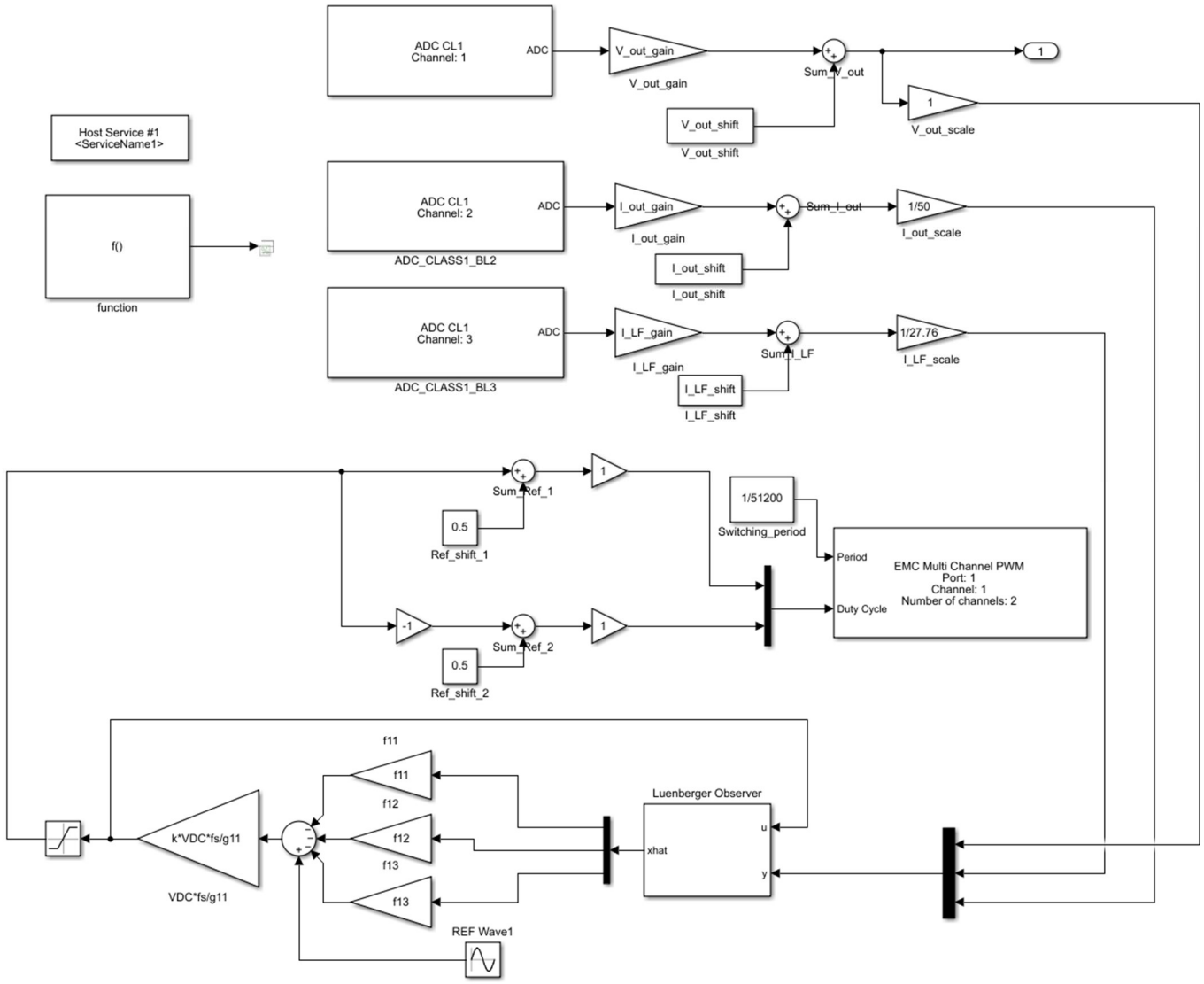


Figure 16. The interior of the function block, when measuring all the state variables and MISO-OSAP-LO controls the output voltage.

The MATLAB/Simulink/dSpace simulation schema is located inside the "function block". For the MISO control with all the space variables in input, the three independent ADCs triggered by PWM events are used. It is organized in the same architecture as in the microprocessor-based control (the PWM calls all the control functions, and in this way, the input frequency of the PWM sets the switching frequency of the whole function block). The interrupt of channel 1 of the first ADC, when data are ready, calls the function block. The MISO controllers, OSAP or PBC, directly calculate control laws. The modulation scheme is from Figure 1. RTI 1202 measures the state variables (output voltage, output current, and inductor current) and drives the H-bridge of the inverter model (Figure 1). The gains R_i and K_v for the PBC controller and the Luenberger observer l_1, l_2, and l_3 gains were adjusted in the admissible ranges to obtain the lowest THD of the output voltage without oscillations. Figures 15 and 16 present the schemas of the MISO-OSAP-LO control for RTI 1202. The idea of calling the function block is the same for all types of inverter control. Figure 17 presents the interior of the function block in the case of MISO-PBC control. The experimental model of VSI No. 1 with Bode plots from Figure 2 was used because it has higher delays, and owing to this is more difficult to control. The whole delay of the measurement channels is about $7T_s$, including analog-to-digital conversion.

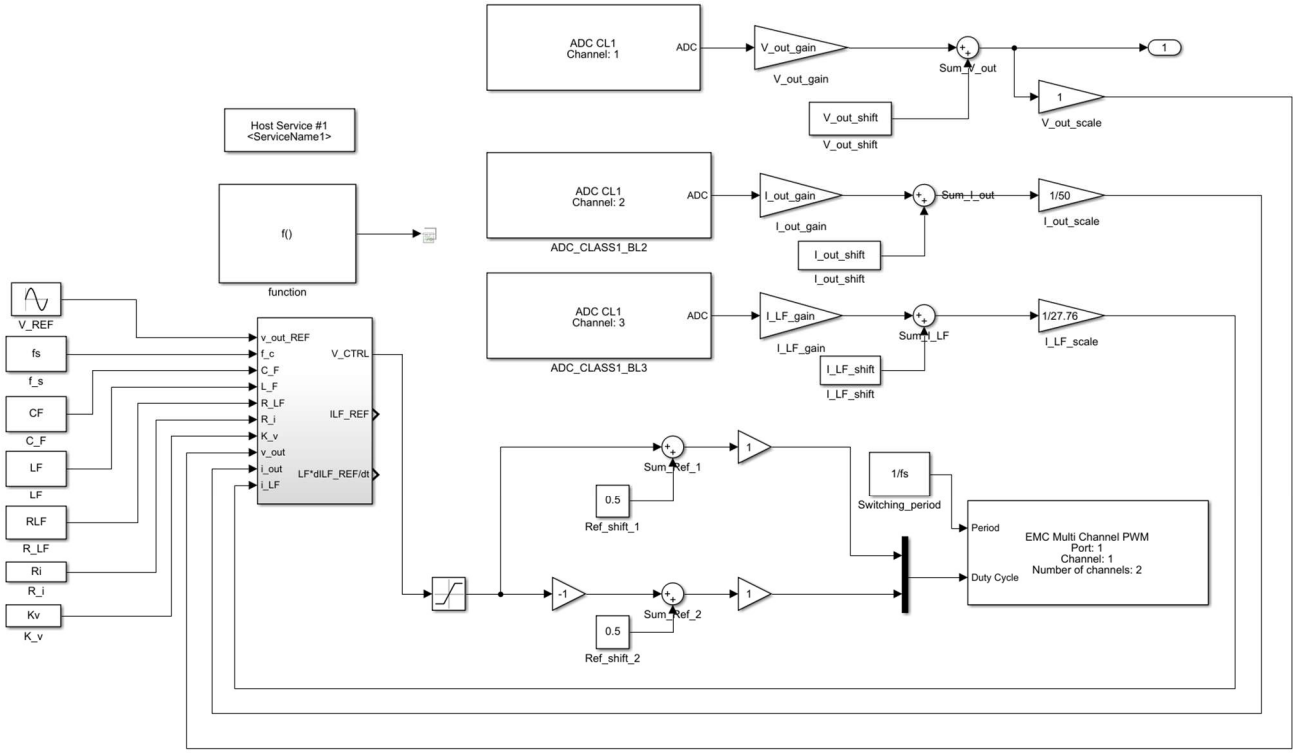
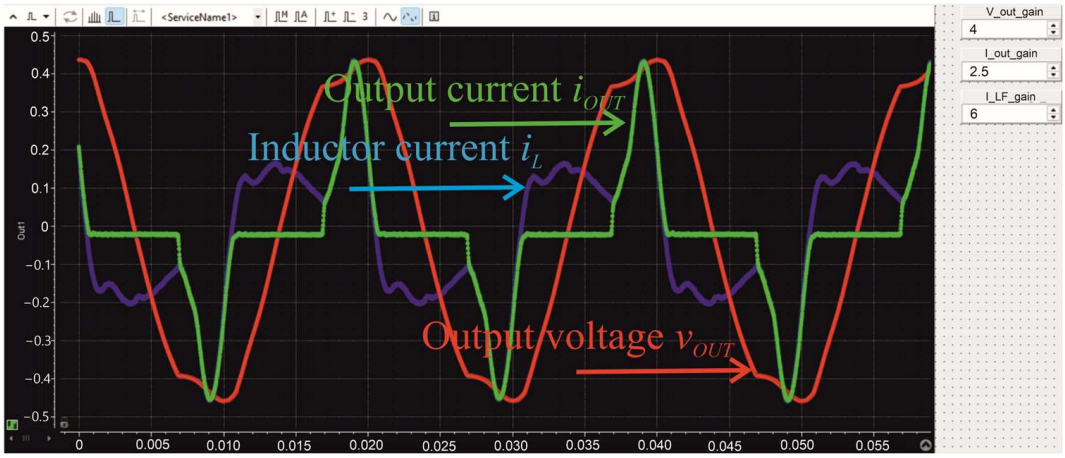
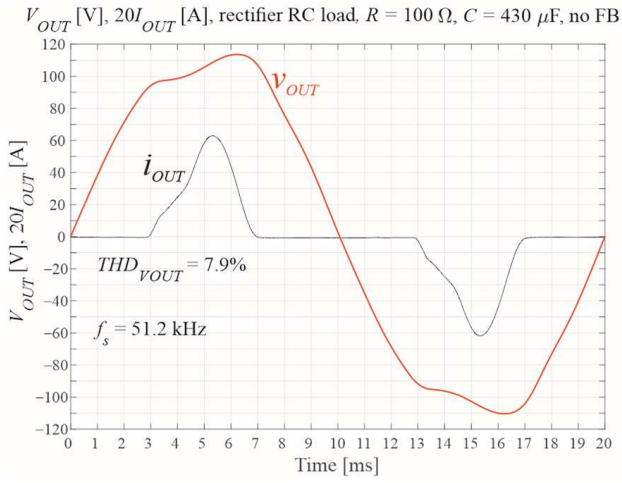


Figure 17. The interior of the function block with measuring all the state variables and MISO-PCB controlling the output voltage.

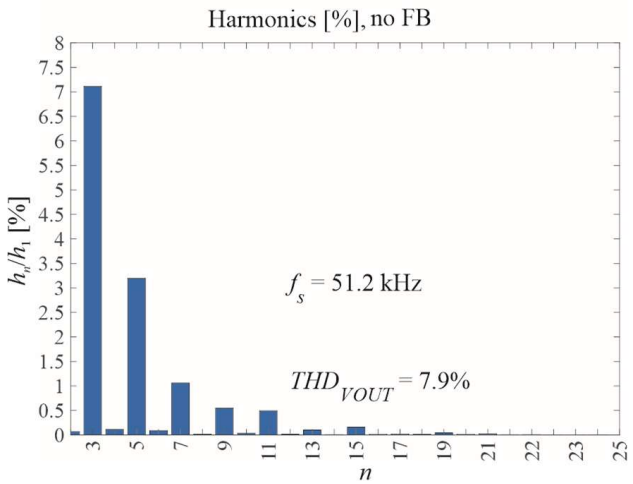
Figure 18a presents the output voltage, output current, and the inductor current waveforms measured by the MicroLabBox, presented by the dSpace ControlDesk 7.5 view. The stored data from the Rigol DS 4014 and the THD calculated in MATLAB 2021b are presented in Figure 18b, and the output voltage harmonic spectrum is presented in Figure 18c. The adequate waveforms for the MIS-OSAP-LO control are presented in Figure 19a–c, and for MISO-PBC control in Figure 20a–c. The parameters for the Luenberger observer in MISO-OSAP-LO control $l_{vOUT} = 0.1$, $l_{iLF} = 0.01$, $l_{iOUT} = 1$, were set experimentally to obtain the lowest THD. The gains $Kv = 1$, $Ri = 30$ were set in the same way (minimum THD) for the MISO-PBC control. The MISO-OSAP control without LO resulted in the oscillations of the output voltage and is not presented. The gains of amplifiers in the MicroLabBox function block were 4 for v_{OUT}, 2.5 for i_{OUT}, and 6 for i_{LF} to obtain the adjustment from Figure 14. The results of the control are presented in Table 2. Figure 21 shows the laboratory station for experimental verification of simulations.



(**a**)



(**b**)

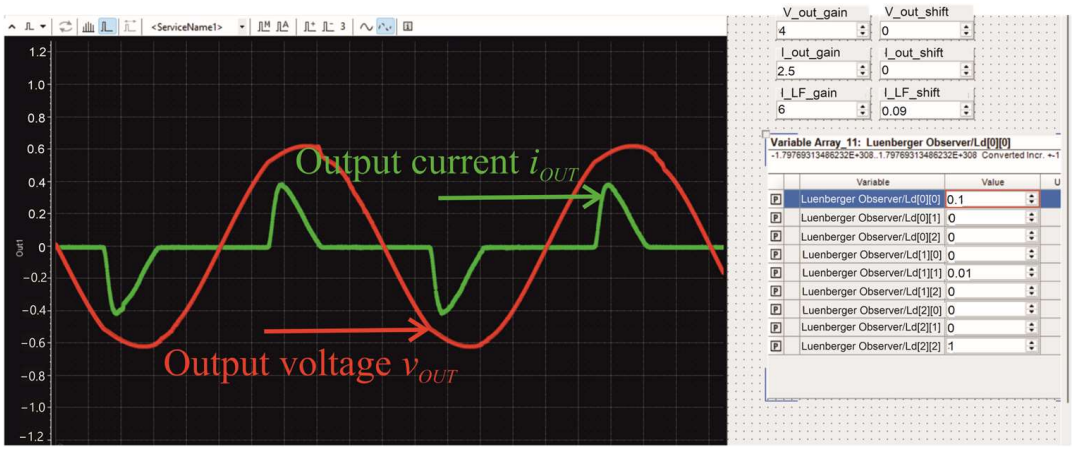


(**c**)

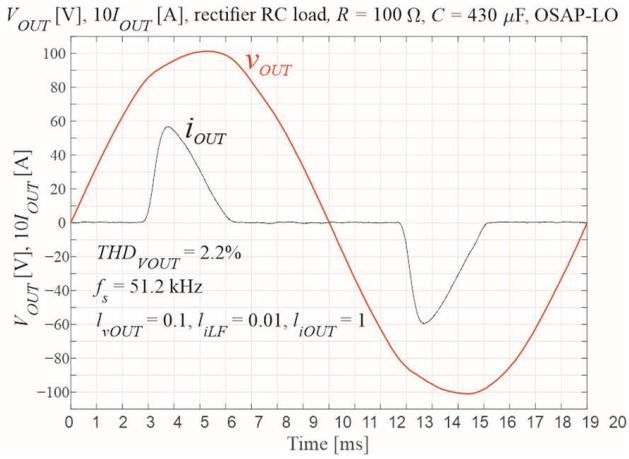
Figure 18. Measured output voltage and current waveforms: (**a**)—dSpace ControlDesk 7.5 view, (**b**)—data from the digital oscilloscope, and (**c**) calculated harmonics of the output voltage of the VSI No. 1 (Figure 2) without feedback for the standard rectifier RC load (f_s = 51,200 Hz, L_F = 2 mH, C_F = 51 μF, R_L = 1 Ω, R_s = 1 Ω, C = 430 μF, R = 100 Ω, PF ≈ 0.7).

Table 2. Output voltage distortions of the experimental VSI No. 1 without feedback, with the MISO-OSAP-LO control and with MISO-PBC control for the rectifier RC load (PF ≈ 0.7).

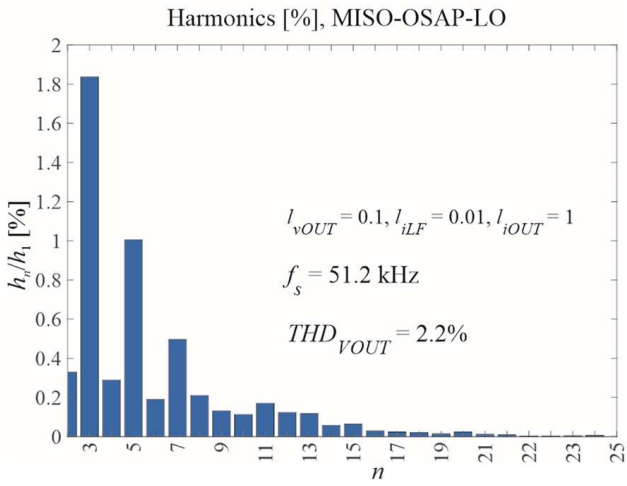
Controller Type	Parameters of Controller	THD [%]
No feedback loop	-	7.9%
MISO-OSAP-LO	$M = 0.8$, $l_{vOUT} = 0.1$, $l_{iLF} = 0.01$, $l_{iOUT} = 1$	2.2%
MISO-PBC	$M = 0.8$, $Kv = 1$, $Ri = 30$	0.87%



(**a**)

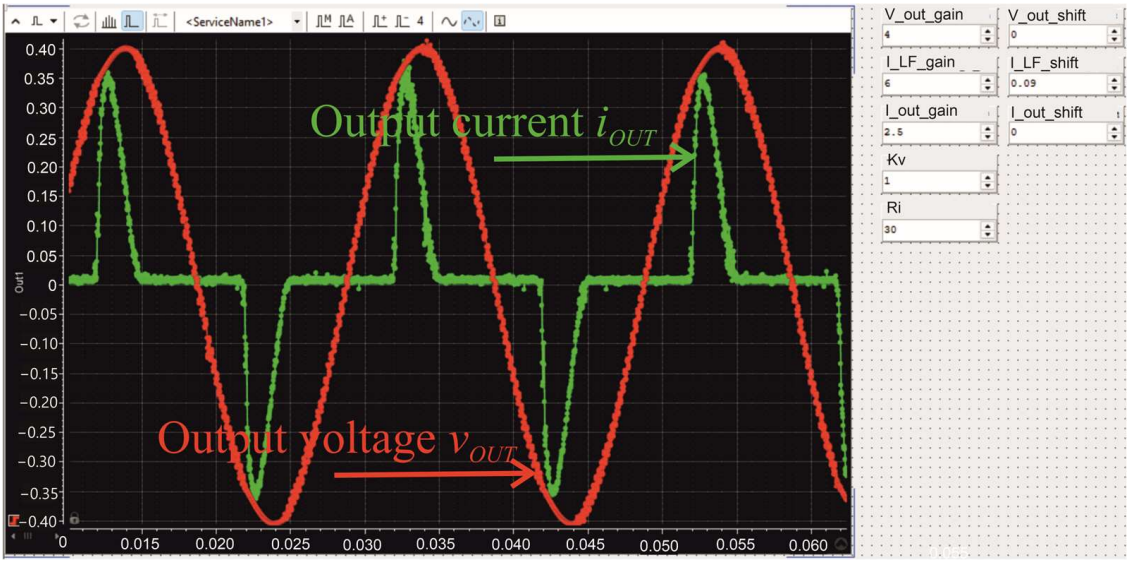


(**b**)

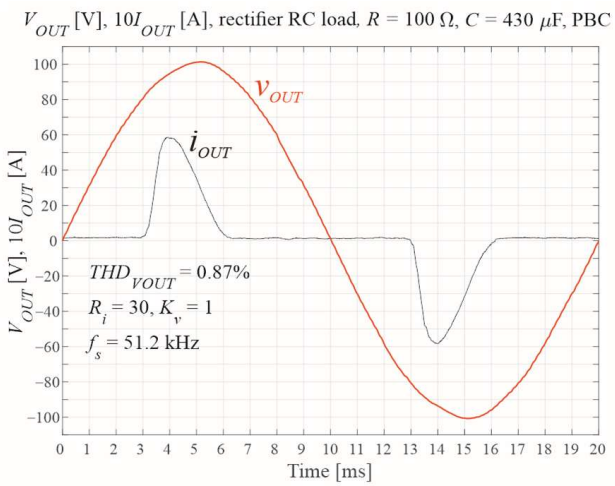


(**c**)

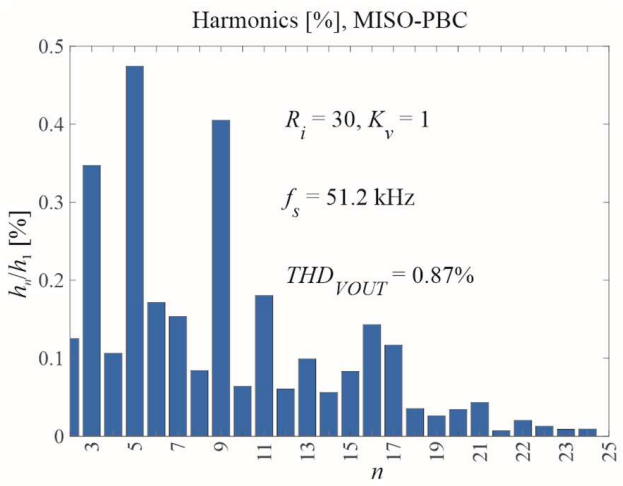
Figure 19. Measured output voltage and current waveforms: (**a**)—dSpace ControlDesk 7.5 view, (**b**)—data from digital oscilloscope, and (**c**) calculated harmonics of the output voltage of the VSI No. 1 (Figure 2) for the MISO-OSAP-LO control ($l_{vOUT} = 0.1$, $l_{iLF} = 0.01$, $l_{iOUT} = 1$) for the standard rectifier RC load (f_s = 51,200 Hz, L_F = 2 mH, C_F = 51 μF, R_L = 1 Ω, R_s = 1 Ω, C = 430 μF, R = 100 Ω).



(**a**)



(**b**)



(**c**)

Figure 20. Output voltage and current waveforms: (**a**)—dSpace ControlDesk 7.5 view, (**b**)—data from digital oscilloscope, and (**c**) calculated harmonics of the output voltage of the VSI No. 1 (Figure 2) for the MISO-PBC control (Kv = 1, Ri = 30) for the standard rectifier load (f_s = 51,200 Hz, L_F = 2 mH, C_F = 51 μF, R_L = 1 Ω, R_s = 1 Ω, C = 430 μF, R = 100 Ω, PF ≈ 0.7).

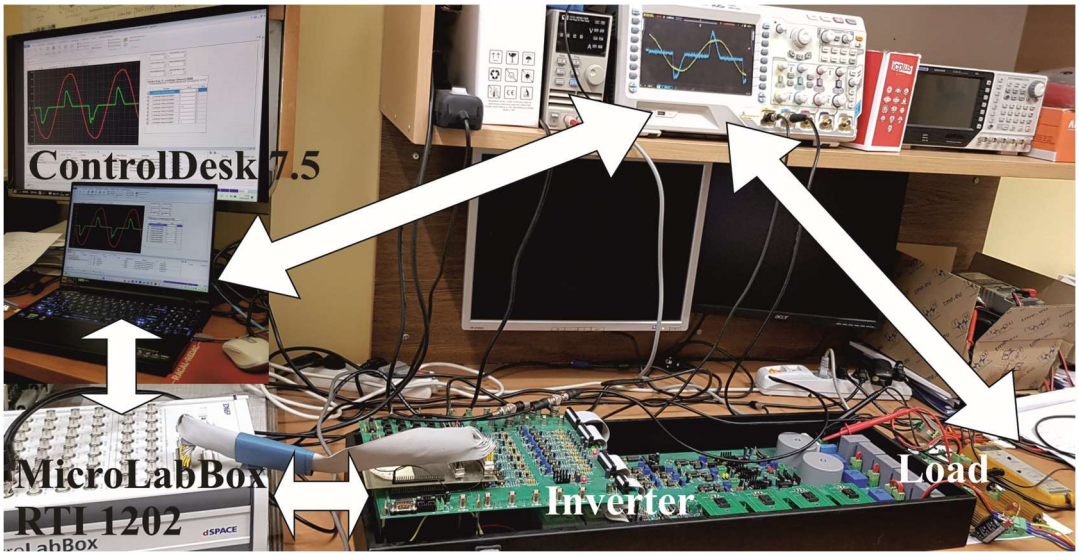


Figure 21. Laboratory station.

8. The Discussion of the Experimental Results

Both types of control were tested for the standard nonlinear load (PF = 0.7). The results of the laboratory VSI No. 1 control (with the whole delay $7T_s$, which is adequate to the additional delay $6T_s$ in simulations, where we have zero-order-hold units simulating analog-to-digital converters in the measuring channels), discrete MISO-OSAP-LO and discretized MISO-PBC types, presented in Table 2, are similar to the simulation results from Table 1. The MISO-OSAP without LO state variables prediction is useless in real systems with delays (it would be perfect for systems without delays) because delays result in oscillations of the output voltage. The idea of PBC control, of the stored energy consideration (Hamiltonian function), makes this control more robust to the low delays in the high switching frequency system. The advantage of the MISO-OSAP that we do not need to set its parameters vanishes when using prediction (we have to adjust Luenberger gains for all the measured state variables). The success of the experiment depends on the proper setting of the gains in the measurement channels. In simulations, setting gains was easy; in the real system, it is always experimentally set, and finally, the gains of the controllers directly depend on the adjusted measurement channels' gains (Figure 14). We can notice that it was possible to adjust higher gains of MISO-PBC in the experimental system than in simulations (Kv = 1, Ri = 30 vs. K_v = 0.2, R_i = 10); however, all the gains were in the admissible area (Figure 10).

9. Conclusions

The paper's goal was to enable the choice between very fast, pure discrete control, MISO-OSAP deadbeat type, with the discretized MISO-PBC control based on the stored energy calculation, for the relatively high switching frequency. It was shown that even for the high switching frequency, MISO-OSAP requires state variable prediction (e.g., Luenberger observer) in the real system with delays. The results of control MISO-OSAP-LO and MISO-PBC are similar, with a slightly lower THD (0.87% vs 2.2%) of the VSI output voltage for MISO-PBC. The reason could be the relatively simple prediction, but in the previous work [55] it was shown that using a more sophisticated Kalman filter does not result in lower distortions of the output voltage. The first advantage of the deadbeat control, that we do not need to calculate any gains of the controller, vanishes in the case of implementing prediction. So, the conclusion is that MISO-PBC is a more useful control type of VSI.

Author Contributions: Conceptualization, Z.R.; methodology, Z.R.; software, Z.R.; validation, Z.R., W.O. and G.W.; formal analysis, Z.R.; investigation, Z.R., W.O. and G.W.; resources, Z.R., W.O. and G.W.; data curation, Z.R., W.O. and G.W.; writing—original draft preparation, Z.R.; writing—review and editing, Z.R., W.O. and G.W.; visualization, Z.R.; supervision, Z.R.; project administration, Z.R.; funding acquisition, Z.R., W.O. and G.W. All authors have read and agreed to the published version of the manuscript.

Funding: This research was partially supported by the Polish Ministry of Education and Science funding for statutory activities (BK-246/RAu-11/2025).

Data Availability Statement: All data files with results of simulations and measurements, the software for VSI simulation, and control of the experimental inverter are in the private possession of the author. The data presented in this study are available on request from the corresponding author due to private concerns.

Acknowledgments: The author would like to thank Andrzej Tutaj of Technika Obliczeniowa sp. z o. o. (www.tobl.com.pl) (accessed on 18 June 2025) for his support in the utilization of MicroLabBox and Krzysztof Bernacki, Department of Electronics, Electrical Engineering and Microelectronics, Faculty of Automatic Control, Electronics and Computer Science, Silesian University of Technology, Gliwice, Poland, for his previous cooperation in inverter control research and his participation in the power electronics laboratory creation.

Conflicts of Interest: The author declares no conflicts of interest.

Abbreviations

The following abbreviations are used in this manuscript:

VSI	Voltage Source Inverter
THD	Total harmonic distortion
MISO	Multi-Input Single-Output
SISO	Single-Input Single-Output
LO	Luenberger observer
OSAP	One-Sample-Ahead Preview
PBC	Passivity-Based Control
RTI	Real-Time Interface
Ts	Switching period
fs	Switching frequency
fm	Fundamental frequency (50 Hz)

References

1. Kawamura, A.; Chuarayapratip, R.; Haneyoshi, T. Deadbeat control of PWM inverter with modified pulse patterns for uninterruptible power supply. *IEEE Trans. Ind. Electron.* **1988**, *35*, 295–300. [CrossRef]
2. Milbradt, D.M.C.; Hollweg, G.V.; da Silveira, P.E.W.B.; Gründling, H. A robust adaptive One Sample Ahead Preview controller for grid-injected currents of a grid-tied power converter with an LCL filter. *Int. J. Electr. Power Energy Syst.* **2022**, *142*, 108286. [CrossRef]
3. Rech, C.; Grundling, H.A.; Pinheiro, J.R. Comparison of discrete control techniques for UPS applications. In Proceedings of the Conference Record of the 2000 IEEE Industry Applications Conference. Thirty-Fifth IAS Annual Meeting and World Conference on Industrial Applications of Electrical Energy (Cat. No.00CH37129), Rome, Italy, 8–12 October 2000; Volume 4, pp. 2531–2537. [CrossRef]
4. Luenberger, D.G. Observing the state of a linear system. *IEEE Trans. Mil. Electron.* **1964**, *8*, 74–80. [CrossRef]
5. Luenberger, D.G. An introduction to observers. *IEEE Trans. Autom. Control* **1971**, *16*, 596–602. [CrossRef]
6. Rymarski, Z.; Bernacki, K. Different Features of Control Systems for Single-Phase Voltage Source Inverters. *Energies* **2020**, *13*, 4100. [CrossRef]
7. *IEC 62040-3:2021*; Uninterruptible Power Systems (UPS)—Part 3: Method of Specifying the Performance and Test Requirements. IEC: Geneva, Switzerland, 2021.
8. Rymarski, Z. The Influence of Switching Frequency on Control in Voltage Source Inverters. *Energies* **2024**, *17*, 4508. [CrossRef]

9. *IEEE 519-2022*; IEEE Standard for Harmonic Control in Electric Power Systems. IEEE: Piscataway, NJ, USA, 2022.
10. Dahono, P.A.; Purwadi, A.; Qamaruzzaman. An LC filter design method for single-phase PWM inverters. In Proceedings of the International Conference on Power Electronics and Drive System, Singapore, 21–24 February 1995; Volume 2, pp. 571–576.
11. Rymarski, Z. The discrete model of the power stage of the voltage source inverter for UPS. *Int. J. Electron.* **2011**, *98*, 1291–1304. [CrossRef]
12. Kim, J.; Choi, J.; Hong, H. Output LC filter design of voltage source inverter considering the performance of controller. In Proceedings of the PowerCon 2000. 2000 International Conference on Power System Technology. Proceedings (Cat. No.00EX409), Perth, WA, Australia, 4–7 December 2000; Volume 3, pp. 1659–1664.
13. Micrometals Alloy Powder Core Catalogue. 2021. Available online: https://micrometals.com/design-and-applications/literature/ (accessed on 10 June 2024).
14. Bernacki, K.; Rymarski, Z.; Dyga, Ł. Selecting the coil core powder material for the output filter of a voltage source inverter. *Electron. Lett.* **2017**, *53*, 1068–1069. [CrossRef]
15. Rymarski, Z.; Bernacki, K.; Dyga, Ł. Measuring the power conversion losses in voltage source inverters. *AEU-Int. J. Electron. Communications* **2020**, *124*, 153359. [CrossRef]
16. Rymarski, Z. *Single-Phase and Three-Phase Voltage Source Inverters Used in UPS Systems*; Wydawnictwo Politechniki Śląskiej: Gliwice, Poland, 2010; ISBN 978-83-7335-642-9.
17. Kim, H.; Sul, S.K. Analysis on output LC filters for PWM inverters. In Proceedings of the 2009 IEEE 6th International Power Electronics and Motion Control Conference, Wuhan, China, 17–20 May 2009; pp. 384–389. [CrossRef]
18. Aman, Y.A.; Datta, A. An Effective Filter Design for Single-Phase Inverters. In Proceedings of the 2023 IEEE Guwahati Subsection Conference (GCON), Guwahati, India, 23–25 June 2023; pp. 1–5. [CrossRef]
19. Treimanis, A.; Apse-Ansītis, P. Optimized Design of Single Phase Inverter Output LC-filter. In Proceedings of the 2019 IEEE 7th IEEE Workshop on Advances in Information, Electronic and Electrical Engineering (AIEEE), Liepaja, Latvia, 15–16 November 2019; pp. 1–5. [CrossRef]
20. Khoshkbar-Sadigh, A.; Dargahi, V.; Lakhera, K.; Corzine, K. Analytical Design of LC Filter Inductance for Two-Level Inverters Based on Maximum Ripple Current. In Proceedings of the IECON 2019—45th Annual Conference of the IEEE Industrial Electronics Society, Lisbon, Portugal, 14–17 October 2019; pp. 1621–1626. [CrossRef]
21. Ahmad, A.A.; Abrishamifar, A.; Farzi, M. A New Design Procedure for Output LC Filter of Single Phase Inverters. In Proceedings of the 3rd International Conference on Power Electronics and Intelligent Transportation System, Shenzhen, China, 13–14 November 2010; Volume 3, pp. 86–91.
22. Van der Broeck, H.W.; Miller, M. Harmonics in DC to AC converters of single phase uninterruptible power supplies. In Proceedings of the 17th International Telecommunications Energy Conference 1995, INTELEC 95, The Hague, The Netherlands, 29 October–1 November 1995; pp. 653–658.
23. Rymarski, Z. Measuring the real parameters of single-phase voltage source inverters for UPS systems. *Int. J. Electron.* **2017**, *104*, 1020–1033. [CrossRef]
24. Rech, C.; Pinheiro, H.; Grundling, H.A.; Hey, H.L.; Pinheiro, J.R. Comparison Of Digital Control Techniques With Repetitive Integral Action for Low Cost PWM Inverters. *IEEE Trans. Power Electron.* **2003**, *18*, 401–410. [CrossRef]
25. Serra, F.M.; De Angelo, C.H.; Forchetti, D.G. IDA-PBC control of a DC-AC converter for sinusoidal three-phase voltage generation. *Int. J. Electron.* **2017**, *104*, 93–110. [CrossRef]
26. Ben-Brahim, L.; Yokoyama, T.; Kawamura, A. Digital control for UPS inverters. In Proceedings of the Fifth International Conference on Power Electronics and Drive Systems, PEDS 2003, Singapore, 17–20 November 2003; Volume 2, pp. 1252–1257.
27. Deng, H.; Srinivasan, D.; Oruganti, R. Modeling and control of single-phase UPS inverters: A survey. In Proceedings of the International Conference on Power Electronics and Drives Systems, PEDS 2005, Kuala Lumpur, Malaysia, 28 November–1 December 2005; Volume 2, pp. 848–853.
28. Borsalani, J.; Dastfan, A. Decoupled phase voltages control of three phase four-leg voltage source inverter via state feedback. In Proceedings of the 2012 2nd International eConference on Computer and Knowledge Engineering (ICCKE), Mashhad, Iran, 18–19 October 2012; pp. 71–76. [CrossRef]
29. Moon, S.; Choe, J.M.; Lai, J.S. Design of a state-space controller employing a deadbeat state observer for ups inverters. In Proceedings of the 2017 Asian Conference on Energy, Power and Transportation Electrification (ACEPT), Singapore, 24–26 October 2017; pp. 1–6. [CrossRef]
30. Hu, C.; Wang, Y.; Luo, S.; Zhang, F. State-space model of an inverter-based micro-grid. In Proceedings of the 2018 3rd International Conference on Intelligent Green Building and Smart Grid (IGBSG), Yilan, Taiwan, 22–25 April 2018; pp. 1–7. [CrossRef]
31. Åström, K.J.; Wittenmark, B. *Computer-Controlled Systems: Theory And Design*, 3rd ed.; Dover Publications Inc.: Mineola, NY, USA, 2011; ISBN 9780486486130.
32. Westphal, L.C. A special control law: Deadbeat control. In *Handbook of Control Systems Engineering*; The Springer International Series in Engineering and Computer Science; Springer: Boston, MA, USA, 2001; Volume 635. [CrossRef]

33. Rymarski, Z.; Bernacki, K. Different approaches to modelling single-phase voltage source inverters for uninterruptible power supply systems. *IET Power Electron.* **2016**, *9*, 1513–1520. [CrossRef]
34. Wang, Z.; Zhou, K.; Li, S.; Yang, Y. Fractional-order time delay compensation in deadbeat control for power converters. In Proceedings of the 2018 IEEE International Power Electronics and Application Conference and Exposition (PEAC), Shenzhen, China, 4–7 November 2018; pp. 1–6. [CrossRef]
35. Itoyama, M.; Natori, K.; Sato, Y. Fast and Stable Current Control Using Deadbeat PI Control with Smith Compensator. In Proceedings of the 2024 13th International Conference on Renewable Energy Research and Applications (ICRERA), Nagasaki, Japan, 9–13 November 2024; pp. 1089–1094. [CrossRef]
36. Li, C.; Shen, S.; Zhang, J.; Guan, M.; Lu, J. Deadbeat Control Based on New State-observer for PWM Rectifier. In Proceedings of the 2006 Chinese Control Conference, Harbin, China, 7–11 August 2006; pp. 1991–1995. [CrossRef]
37. Zhang, B.; Zuo, Y.; Quan, L.; Zhu, X. Deadbeat Active Disturbance Rejection Controller for the Current Control of Electric Drives in the Presence of Two-step Delay. In Proceedings of the 2022 IEEE 5th International Electrical and Energy Conference (CIEEC), Nangjing, China, 27–29 May 2022; pp. 1924–1928. [CrossRef]
38. Davis, J.H. Luenberger Observers. In *Foundations of Deterministic and Stochastic Control*; Systems & Control: Foundations & Applications; Birkhäuser: Boston, MA, USA, 2002; pp. 245–254. [CrossRef]
39. Saoudi, M.; Hani, B.; Aissa, C. Efficient Deadbeat Control of Single-Phase Inverter with Observer for High Performance Applications. *Prz. Elektro Tech.* **2023**, *99*, 237. [CrossRef]
40. Fan, H.; Li, Z.; Rodriguez, J.; Wang, B. Model Free Predictive Current Control for Voltage Source Inverter using Luenberger Observer. In Proceedings of the 2023 IEEE International Conference on Predictive Control of Electrical Drives and Power Electronics (PRECEDE), Wuhan, China, 16–19 June 2023; pp. 1–6. [CrossRef]
41. Heydaridoostabad, H.; Ghazi, R. A new approach to design an observer for load current of UPS based on Fourier series theory in model predictive control system. *Int. J. Electr. Power Energy Syst.* **2018**, *104*, 898–909. [CrossRef]
42. Li, J.; Sun, Y.; Li, X.; Xie, S.; Lin, J.; Su, M. Observer-Based Adaptive Control for Single-Phase UPS Inverter Under Nonlinear Load. *IEEE Trans. Transp. Electrif.* **2022**, *8*, 2785–2796. [CrossRef]
43. Montagner, V.F.; Carati, E.G.; Grundling, H.A. An adaptive linear quadratic regulator with repetitive controller applied to uninterruptible power supplies. In Proceedings of the Industry Applications Conference 2000, Rome, Italy, 8–12 October 2000; Volume 4, pp. 2231–2236.
44. Xianghong, Z.; Jianguo, L.; Zhiyong, Z.; Tianhong, M. The Passivity-based Control with Luenberger State Observer of Three-phase Grid Connected Converter. In Proceedings of the 2024 12th International Conference on Smart Grid and Clean Energy Technologies (ICSGCE), Jilin, China, 8–20 October 2024; pp. 1–7. [CrossRef]
45. Stoicuta, O. A New Gain Matrix of the Luenberger Observer for the Vector Control Systems with Induction Motors. In Proceedings of the 2021 International Conference on Electromechanical and Energy Systems (SIELMEN), Iasi, Romania, 6–8 October 2021; pp. 029–034. [CrossRef]
46. Bakhti, I.; Chaouch, S.; Makouf, A.; Douadi, T. Robust sensorless sliding mode control with Luenberger observer design applied to permanent magnet synchronous motor. In Proceedings of the 2016 5th International Conference on Systems and Control (ICSC), Marrakesh, Morocco, 25–27 May 2016; pp. 204–210. [CrossRef]
47. Komurcugil, H. Improved passivity-based control method and its robustness analysis for single-phase uninterruptible power supply inverters. *IET Power Electron.* **2015**, *8*, 1558–1570. [CrossRef]
48. Ortega, R.; Perez, J.A.L.; Nicklasson, P.J.; Sira-Ramirez, H. *Passivity-Based Control of Euler-Lagrange Systems: Mechanical, Electrical and Electromechanical Applications (Communications and Control Engineering)*; Springer: London, UK, 1998.
49. Wang, Z.; Goldsmith, P. Modified energy-balancing-based control for the tracking problem. *IET Control Theory Appl.* **2008**, *2*, 310–312. [CrossRef]
50. Ortega, R.; Garcia-Canseco, E. Interconnection and Damping Assignment Passivity-Based Control: A Survey. *Eur. J. Control* **2004**, *5*, 432–450. [CrossRef]
51. Ortega, R.; Garcia-Canseco, E. Interconnection and Damping Assignment Passivity-Based Control: Towards a Constructive Procedure—Part I. In Proceedings of the 43rd IEEE Conference on Decision and Control, Nassau, Bahamas, 14–17 December 2004; pp. 3412–3417. [CrossRef]
52. Ortega, R.; Espinosa-Perez, G. Passivity-based control with simultaneous energy-shaping and damping injection: The induction motor case study. *IFAC Proc.* **2005**, *38*, 477–482. [CrossRef]
53. Khefifi, N.; Houari, A.; Ait-Ahmed, M.; Machmoum, M.; Ghanes, M. Robust IDA-PBC based Load Voltage Controller for Power Quality Enhancement of Standalone Microgrids. In Proceedings of the IEEE IECON 2018—44th Annual Conference of the IEEE Industrial Electronics Society, Washington, DC, USA, 21–23 October 2018; pp. 249–254. [CrossRef]

54. Rymarski, Z.; Bernacki, K. Technical Limits of Passivity-Based Control Gains for a Single-Phase Voltage Source Inverter. *Energies* **2021**, *14*, 4560. [CrossRef]
55. Rymarski, Z. Improving Low-Frequency Digital Control in the Voltage Source Inverter for the UPS System. *Electronics* **2024**, *13*, 1469. [CrossRef]

Disclaimer/Publisher's Note: The statements, opinions and data contained in all publications are solely those of the individual author(s) and contributor(s) and not of MDPI and/or the editor(s). MDPI and/or the editor(s) disclaim responsibility for any injury to people or property resulting from any ideas, methods, instructions or products referred to in the content.